PROCEEDINGS A

royalsocietypublishing.org/journal/rspa

Research

Cite this article: Su W, E X, Jing Z, Chen SX. 2026 Glider path design and control for reconstructing three- dimensional structures of oceanic mesoscale eddies. *Proc. R. Soc. A* **482**: 20250533.
https://doi.org/10.1098/rspa.2025.0533

Received: 18 June 2025
Accepted: 16 January 2026

Subject Areas:
statistics

Keywords:
sparse sampling design, online adaptive control, spatio-temporal field reconstruction

Author for correspondence:
Song Xi Chen
e-mail: sxchen@tsinghua.edu.cn

Electronic supplementary material is available online at https://doi.org/10.6084/m9.figshare.c.8316008.

THE ROYAL SOCIETY PUBLISHING

Glider path design and control for reconstructing three-dimensional structures of oceanic mesoscale eddies

Wu Su[1], Xiaoyuan E[2], Zhao Jing[3,4] and Song Xi Chen[5]

[1]Center for Big Data Research, Peking University, Beijing 100871, People's Republic of China
[2]JD Logistics, Beijing 100176, People's Republic of China
[3]Frontiers Science Center for Deep Ocean Multispheres and Earth System and Key Laboratory of Ocean Dynamics/ Academy of Future Ocean, Ocean University of China, Qingdao 266100, People's Republic of China
[4]Department of Ocean Big Data and Prediction, Laoshan Laboratory, Qingdao 266237, People's Republic of China
[5]Department of Statistics and Data Science, Tsinghua University, Beijing 100084, People's Republic of China

SXC, 0000-0002-2338-0873

Underwater gliders are autonomous *in situ* platforms used in oceanographic research. We focus on their application to reconstructing the three-dimensional hydrographic structure of mesoscale eddies by addressing three challenges: efficiently interpolating glider-sampled data, optimally designing glider travel paths, and adaptively controlling glider trajectories in the presence of ocean currents. We develop a thin plate spline (TPS) interpolation scheme with a blocking strategy that significantly reduces computational cost while preserving accuracy. We then formulate a path design procedure to identify trajectory configurations that minimize reconstruction error. Finally, we propose an adaptive control algorithm that enables gliders to travel along the designed paths under realistic oceanic conditions. Evaluations based on a simulated and a real eddy show that the TPS-based interpolation produces more accurate temperature and salinity fields than existing methods, while the designed path configurations effectively balance spatial coverage and sampling efficiency. The adaptive control algorithm enables gliders to maintain

designated trajectories and ensure safe return even under strong currents. Our study shows that the proposed glider design and control framework can be used to advancing *in situ* observing capabilities for eddies and complex ocean process reconstruction.

1. Introduction

The mesoscale eddy is one of the dominant forms of motion in the ocean, with a diameter ranging from tens to hundreds of kilometres and a vertical depth of hundreds to thousands of meters [1]. The study of the three-dimensional hydrographic field of mesoscale eddies is a major issue in oceanography and marine science with great significance in the study of climate, marine ecosystems and the environment [2–10].

Although the spatial resolution of state-of-the-art ocean general circulation models has become fine enough to resolve mesoscale eddies owing to increased computational capacity [11], they still cannot accurately simulate mesoscale eddies [12,13]. Simulating a particular mesoscale eddy is even more challenging owing to its turbulent properties and a strong dependence on initial and boundary conditions. Remote sensing-based measurements can only capture the surface footprint of mesoscale eddies, such as eddy-induced sea surface height (SSH) and temperature anomalies [14]. The surface eddy signals can be used to infer the three-dimensional structure of mesoscale eddies [15–18]. For instance, Zhang *et al.* [19] suggested that the vertical structure of mesoscale eddies can be universally represented by a sinusoidal function in a stretched coordinate depending on the ratio of buoyancy frequency to Coriolis frequency. Isern-Fontanet *et al.* [20] reconstructed the three-dimensional structure of mesoscale eddies using the sea surface temperature (SST) from satellite observations based on a surface quasi-geostrophic framework. However, this framework underpinning the reconstruction was likely an oversimplification of the real ocean. Furthermore, the satellite-based reconstruction was usually performed for seawater density rather than temperature and salinity themselves, which cannot be directly inferred without assuming a specific temperature–salinity relationship.

Controllable and autonomous ocean *in situ* observation platforms provide an alternative form of eddy observation by actively collecting the hydrographic data within mesoscale eddies. These data can then be used for reconstructing the eddy's three-dimensional hydrographic field. An underwater glider (UG) is an autonomous underwater vehicle that propels itself by periodically adjusting its buoyancy to ascend and descend, while its fixed wings convert this vertical motion into forward movement. In this way, gliders navigate through buoyancy-driven propulsion rather than ocean currents, even though currents may affect their actual paths. Their design allows for extremely high energy efficiency and long endurance, making them well suited for extended autonomous missions. Moreover, they are highly versatile platforms capable of carrying a wide range of sensors to measure physical, chemical, biological and environmental parameters, thereby supporting a diverse range of multidisciplinary oceanographic studies [21–23].

The gliders collect data such as seawater temperature and salinity at high temporal resolution along designed paths. Although the glider's sampling locations can, in rare cases, be directly calculated when the glider is equipped with specialized sensors which record the underwater velocity of the vehicle, in most deployments, such sensors are not available. This means that the sampling locations have to be estimated using theoretical flight models in combination with onboard sensor data (pitch, heading, depth) and periodic GPS information when the gliders surface.

Owing to their relatively low cost and large spatial coverage, UGs have been widely used to observe the three-dimensional hydrographic structure of mesoscale eddies, and the growing demand for high-resolution reconstruction of mesoscale eddies has led to an increasing number of deployments.

There are three key issues in the efficient use of ocean gliders. The first is to develop computationally efficient interpolation methods to reconstruct the three-dimensional

hydrographic field of a mesoscale eddy from sparse observations. The second concerns the design of glider travel paths that can provide well-distributed sampling for accurate reconstruction. The third is to control gliders to follow the designed paths reliably in the presence of ocean currents. To our knowledge, there have been no systematic solutions to these issues in the existing research.

A popular method for reconstructing mesoscale eddies is the spatial interpolation based on smooth two- or three-dimensional interpolation functions [20,24]. Shepard [25] proposed the inverse distance weighted (IDW) interpolation, which assigns larger weights to closer observations. Another commonly used spatial interpolation method is the Kriging [26–29], which is a statistical method that utilizes the spatial dependence for best linear unbiased interpolation. The IDW and Kriging methods are widely used in geology and atmospheric science, and the IDW interpolation has also been applied to three-dimensional eddy reconstruction [30].

Interpolation with spline functions is another method, which fits a piecewise function through observation points with certain smoothness conditions [31]. Wahba & Wendelberger [32] introduced spline interpolations to spatial analysis in meteorology, and in particular the thin plate spline (TPS). Hutchinson & Gessler [33] proved that there is a mathematical connection between the TPS and the Kriging and pointed out that the TPS using generalized cross-validation (GCV) to select the roughness penalty parameters may be more efficient than Kriging. Zheng & Basher [34] proposed a method to select tuning parameters by minimizing the mean square error, which further improved the performance of the TPS interpolation.

For glider path design, previous studies tended to focus on minimizing two-dimensional reconstruction errors. For a circular glider formation, Leonard *et al.* [35] derived a glider path scheme with minimal expected reconstruction error at the sea surface. Alvarez *et al.* [36] combined gliders with a network of floats to calculate the optimal path design for up to three gliders using a genetic algorithm to minimize the average error of the reconstructed field. A combination of mooring systems with gliders was considered in [37].

Existing studies on glider path control mostly aimed at reaching the destination in the least amount of time with minimal energy consumption, while paying little attention to path design or reconstruction quality. As the glider's movement is affected by ocean currents, control methods such as the proportional–integral–derivative (PID) controller have been used in attitude control of gliders. Sang *et al.* [38] proposed a hybrid heading control algorithm that integrated an adaptive fuzzy incremental PID with an anti-saturation compensation strategy to achieve robust heading control. Other studies considered minimizing the travel time or energy consumption [39]. Besada-Portas *et al.* [40] applied the particle swarm optimization algorithm to glider path control. The feasibility of applying the differential evolution (DE) algorithm to the task of minimizing glider travel time was demonstrated in previous studies [41–44]. In addition, reinforcement learning methods had been considered recently [45,46], in which the spatial domain was discretized into grid points, which inevitably caused a loss of resolution, and their applicability to high-resolution applications remains to be investigated. Furthermore, these approaches required knowledge of the current field and did not consider glider control along designed paths.

This article addresses three major issues with the use of gliders for data collection for reconstructing the hydrographic field of a mesoscale eddy. We first demonstrate that the TPS is an effective interpolation method for eddy reconstruction and propose a three-dimensional blocking scheme to enhance the TPS computation on glider-sampled data. Second, we propose a data-driven glider path design method to find the best formation pattern such that the data collected along this formation yield the smallest reconstruction error. After having designed the glider travel paths, we consider glider control to ensure that they stay on the designed paths as much as possible in the presence of ocean current. We devise an objective function that is a weighted sum of the glider's absolute deviation to the designated pathway and the distance to the final destination with the weights being adjustable according to the direction and the magnitude of the ocean current. Having the distance to the destination in the objective function is to prevent the glider being stuck or lost under strong ocean current, which can happen if the objective function is only based on the deviation to the designed path, given the limited force

available to the gliders. Eight optimization algorithms, including DE and self-adaptive DE (JDE), were tested on a simulated eddy with observed ocean current, and the algorithms yielding the most stable path control were identified.

The rest of the article is organized as follows. Section 2 introduces TPS interpolation and proposes a three-dimensional blocking interpolation method for rapid reconstruction of the hydrographic field of an eddy. Sections 3 and 4 present the proposed glider path design and path control methods, respectively. Experimental results on the simulated eddy are presented in §§5 and 6, followed by validation on real eddies in §7. The article concludes with a summary of findings in §8. Additional technical and numerical details are given in the supplementary material (SM).

2. Interpolation for hydrographic reconstruction

This section presents the TPS-based method for reconstructing the hydrographic field using sampled data from the gliders and proposes a three-dimensional blocking algorithm to speed up the TPS computation. Figure 1 displays the hydrographic structure of a simulated eddy, which shows strong three-dimensional spatial dependence.

(a) Thin plate spline

Wahba & Wendelberger introduced the TPS interpolation for spatial data analysis in meteorology [32]. Hijmans *et al*. [47] employed the TPS to interpolate meteorological variables over global land area to achieve higher spatial resolution at the time.

Consider the glider-sampled data points $(\boldsymbol{X}_i, Y_i), i = 1, 2, \ldots, n$. Here, $\boldsymbol{X}_i$ denotes the three-dimensional spatial coordinate (longitude, latitude, depth) at which a glider measurement Y_i was taken, where Y_i can represent either temperature or salinity. The measurements Y_i are modelled as $Y_i = f(\boldsymbol{X}_i) + \epsilon_i$, where the measurement errors $\{\epsilon_i\}_{i=1}^n$ are independent and identically distributed zero-mean random variables with finite variance σ_ϵ^2. The goal is to estimate the underlying smooth function $f(\cdot)$ from noisy observations collected by gliders.

To obtain a stable estimate of $f(\cdot)$, we adopt the TPS approach, which seeks a function $f^*(\mathbf{x})$ at $\mathbf{x} = (x^{(1)}, \ldots, x^{(p)})^T$ that minimizes the sum of squared interpolation errors along with the bending energy which quantifies the smoothness of a surface [48], namely,

$$\mathcal{J}_n(f) = \sum_{i=1}^{n} (Y_i - f(\boldsymbol{X}_i))^2 + \lambda \int_{\mathcal{R}^p} \left(\sum_{i=1}^{p} \sum_{j=1}^{p} \left(\frac{\partial^2 f}{\partial x^{(i)} x^{(j)}} \right)^2 \right) \mathrm{d}x^{(1)} \cdots \mathrm{d}x^{(p)}. \tag{2.1}$$

The aforementioned integral is the second-order bending energy of f, and $\lambda > 0$ is a smoothing parameter. A larger (smaller) λ results in a smoother (rougher) interpolation function.

This leads to the optimization problem $\min_f \mathcal{J}_n(f)$. As shown in Section S1 in the electronic supplementary material, the minimizer f^* is

$$f^*(\mathbf{x}) = \beta_0 + \sum_{k=1}^{p} \beta_k x^{(k)} + \sum_{i=1}^{n} w_i G_p(\|\mathbf{x} - \boldsymbol{X}_i\|_2), \tag{2.2}$$

where

$$G_p(r) = \begin{cases} r^{4-p} \ln r, & p = 2, 4; \\ r^{4-p}, & \text{otherwise} \end{cases}, \tag{2.3}$$

and the coefficients $\beta = (\beta_0, \beta_1, \ldots, \beta_p)^T$ and the weights $w = (w_1, \ldots, w_n)^T$ are to be estimated. Derivations given in the electronic supplementary material show that the estimates of $\boldsymbol{\beta}$ and $\mathbf{w}$

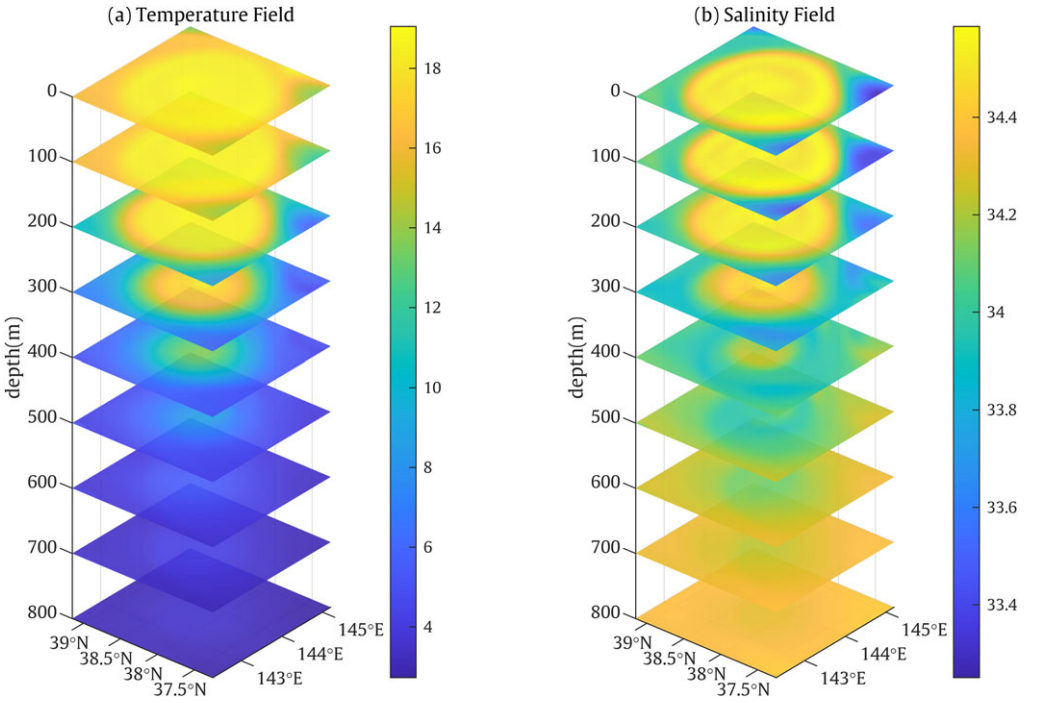

Figure 1. Three-dimensional structure of the temperature (°C) and salinity (psu) fields of a simulated mesoscale eddy, where the three axes represent longitude, latitude and depth, respectively.

can be obtained by solving

$$\begin{bmatrix} \mathbf{A} + \lambda I, & \mathbf{X} \\ \mathbf{X}^T, & O \end{bmatrix} \begin{pmatrix} \mathbf{w} \\ \boldsymbol{\beta} \end{pmatrix} = \begin{pmatrix} \mathbf{Y} \\ \mathbf{0} \end{pmatrix}, \tag{2.4}$$

where $\mathbf{Y} = (Y_1, \ldots, Y_n)^T$, $\mathbf{X}$ is a matrix with the ith row being $[1, \mathbf{X}_i^T]$, for $i = 1, 2, \ldots n$, and $\mathbf{A} = (a_{ij})$ is an $n \times n$ matrix with entries $a_{ij} = G_p(\|\boldsymbol{X}_i - \boldsymbol{X}_j\|_2)$ for $i \neq j$ and $a_{ii} = 0$.

Let $\hat{\boldsymbol{\beta}}$ and $\hat{\mathbf{w}}$ be the estimates after solving equation (2.4). Suppose one wants to interpolate the value of the hydrographic variable Y_0 at a coordinate $\boldsymbol{X}_0 = (X_{0,1}, X_{0,2}, X_{0,3})$. The interpolation by the TPS is given as follows:

$$\hat{Y}_0 = f^*(\boldsymbol{X}_0) = \hat{\beta}_0 + \hat{\beta}_1 X_{0,1} + \hat{\beta}_2 X_{0,2} + \hat{\beta}_3 X_{0,3} + \sum_{i=1}^{n} \hat{w}_i r_{0i}, \tag{2.5}$$

where r_{0i} is the Euclidean distance between $\boldsymbol{X}_0$ and $\boldsymbol{X}_i$.

Although we perform a three-dimensional reconstruction, we find that using the two-dimensional Green's function $G_2(r) = r^2 \ln r$ brings better empirical results than those using the three-dimensional counterpart, which was also noted in other studies [49,50]. This may be owing to the fact that although the purpose is for the three-dimensional reconstruction, mesoscale eddies exhibit a pronounced scale disparity, with horizontal dimensions spanning tens to hundreds of kilometres, while the vertical extents are typically only a few hundred meters [51,52]. In addition, our sampling design is largely two-dimensional via line segments with respect to sea surface. Hence, we use the two-dimensional Green's function in this study.

As discussed in [53], the TPS framework allows for estimating prediction uncertainty at an unsampled location $\boldsymbol{X}_0$. Let $\boldsymbol{\Phi}_0 = (G_p(||\boldsymbol{X}_1 - \boldsymbol{X}_0||_2), \ldots, G_p(||\boldsymbol{X}_n - \boldsymbol{X}_0||_2), \hat{\boldsymbol{\beta}}^T)^T$. The prediction

variance is given as follows:

$$\mathrm{Var}[f^*(X_0)] = \sigma_\epsilon^2 \left(1 + \boldsymbol{\Phi}_0^T \begin{pmatrix} \mathbf{A} + \lambda I & \mathbf{X} \\ \mathbf{X}^T & O \end{pmatrix}^{-1} \boldsymbol{\Phi}_0\right). \tag{2.6}$$

At this stage, all quantities in the expression are known once the TPS interpolation function $f^\star$ has been estimated, with the measurement-error variance σ_ϵ^2 being the only remaining unknown. As σ_ϵ^2 can be estimated from the residuals of the fitted TPS model, the variance in (2.6) can be readily estimated, which provides a measure of the prediction uncertainty and enables the construction of confidence intervals for the reconstructed field.

(b) Blocking strategy for efficient computation

Note that the time complexity for solving the linear system (2.4) is $\mathcal{O}(n^3)$ since $p \ll n$. As the number of data records collected by gliders usually exceeds 100 000 measurement points during an oceanic field campaign, TPS interpolation would endure a heavy computational burden. Indeed, as pointed out by [34], the number of observations for conventional TPS interpolation is better to be less than 1000 to ensure computation feasibility. Hence, it is necessary to develop a computationally efficient algorithm for timely TPS interpolation of an eddy's three-dimensional temperature or salinity field.

We propose a blocking strategy, which divides the entire three-dimensional reconstruction space into overlapping cuboids. For convenience, the study area R is assumed to be a unit cube with unit edge length, which can be realized by the min–max scaling, namely, $x_i^* = (x_i - \min\{x_i\})/(\max\{x_i\} - \min\{x_i\})$, so that $R = \{(x_1, x_2, x_3) \mid 0 \le x_1, x_2, x_3 \le 1\}$, where x_1, x_2 and x_3 represent the standardized longitude, latitude and depth. We divide the unit interval $[0, 1]$ corresponding to each dimension to form multiple sub-cuboids. Let $B_{\mathrm{long}}, B_{\mathrm{lat}}$ and B_{dep} be the number of blocks in longitude, latitude and depth, respectively. For example, for the longitude dimension, the ith sub-interval with an overlapping ratio c is $[E^L_{\mathrm{long},i}, E^U_{\mathrm{long},i}], i = 1, 2, \ldots, B_{\mathrm{long}}$, where

$$\left.\begin{aligned} E^L_{\mathrm{long},i} &= \max\left\{0, \frac{i - 1 - (c/2)}{B_{\mathrm{long}}}\right\}, \\ \text{and} \quad E^U_{\mathrm{long},i} &= \min\left\{1, \frac{i + (c/2)}{B_{\mathrm{long}}}\right\}, \end{aligned}\right\} \tag{2.7}$$

while $\left[E^L_{\mathrm{lat},i}, E^U_{\mathrm{lat},i}\right]$ and $\left[E^L_{\mathrm{dep},i}, E^U_{\mathrm{dep},i}\right]$ can be defined similarly. Then, the cube R is divided into $B = B_{\mathrm{long}} \cdot B_{\mathrm{lat}} \cdot B_{\mathrm{dep}}$ sub-cuboids, denoted as follows:

$$R_{ijk} = \left[E^L_{\mathrm{long},i}, E^U_{\mathrm{long},i}\right] \times \left[E^L_{\mathrm{lat},j}, E^U_{\mathrm{lat},j}\right] \times \left[E^L_{\mathrm{dep},k}, E^U_{\mathrm{dep},k}\right], \tag{2.8}$$

for $i = 1, \ldots, B_{\mathrm{long}}$; $j = 1, \ldots, B_{\mathrm{lat}}$; $k = 1, \ldots, B_{\mathrm{dep}}$.

We first build the TPS interpolation function $\hat{f}_{ijk}(\mathbf{x})$ using all the sampled observations in the sub-cuboid R_{ijk}. The final interpolation function is a weighted average of $\hat{f}_{ijk}(\mathbf{x})$ over all the sub-cuboids $\{R_{ijk}\}$:

$$\hat{f}(\mathbf{x}) = \sum_{i=1}^{B_{\mathrm{long}}} \sum_{j=1}^{B_{\mathrm{lat}}} \sum_{k=1}^{B_{\mathrm{dep}}} \omega_{ijk}(\mathbf{x}) \hat{f}_{ijk}(\mathbf{x}), \tag{2.9}$$

where the weights $\omega_{ijk}(\mathbf{x})$ are determined as follows. Let $\mathbf{x} = (x_1, x_2, x_3)$ be the location where the interpolation is made. For all R_{ijk} that contain $\mathbf{x}$, define

$$\left.\begin{aligned} s_{\mathrm{long},ijk}(\mathbf{x}) &= \min\left\{|x_1 - E^L_{\mathrm{long},i}|, |x_1 - E^U_{\mathrm{long},i}|\right\}, \\ s_{\mathrm{lat},ijk}(\mathbf{x}) &= \min\left\{|x_2 - E^L_{\mathrm{lat},j}|, |x_2 - E^U_{\mathrm{lat},j}|\right\} \\ \text{and} \quad s_{\mathrm{dep},ijk}(\mathbf{x}) &= \min\left\{|x_3 - E^L_{\mathrm{dep},k}|, |x_3 - E^U_{\mathrm{dep},k}|\right\}, \end{aligned}\right\} \tag{2.10}$$

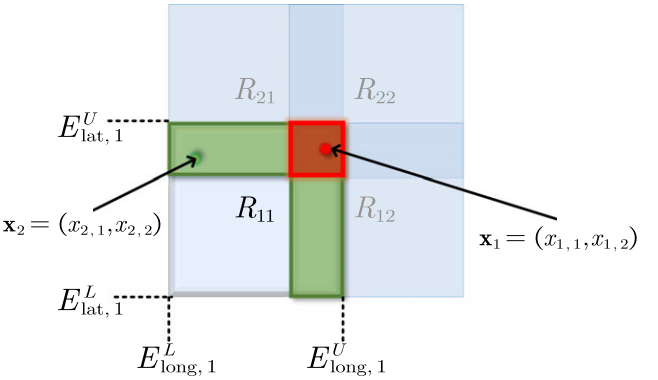

Figure 2. Two-dimensional demonstration of the blocking scheme. For R_{11}, the green parts are the overlaps of two regions and the red part is the overlap of four regions. $d_{11}(\mathbf{x}_1) = |x_{1,1} - E^U_{\text{long},1}||x_{1,2} - E^U_{\text{lat},1}|$, $d_{11}(\mathbf{x}_2) = |x_{2,1} - E^L_{\text{long},1}||x_{2,2} - E^U_{\text{lat},1}|$ and $d_{12}(\mathbf{x}_2) = d_{22}(\mathbf{x}_2) = 0$.

which measure the shortest distance from $\mathbf{x}$ to the boundaries of R_{ijk}. Furthermore, let

$$d_{ijk}(\mathbf{x}) = \begin{cases} s_{\text{long},ijk}(\mathbf{x}) \cdot s_{\text{lat},ijk}(\mathbf{x}) \cdot s_{\text{dep},ijk}(\mathbf{x}), & \mathbf{x} \in R_{ijk}, \\ 0, & \mathbf{x} \notin R_{ijk}. \end{cases} \tag{2.11}$$

Figure 2 illustrates a two-dimensional blocking scheme example and how $d(\mathbf{x})$ is calculated.

After obtaining $d_{ijk}(\mathbf{x})$, the weights

$$\omega_{ijk}(\mathbf{x}) = \frac{d^2_{ijk}(\mathbf{x})}{\sum_{u=1}^{B_{\text{long}}} \sum_{v=1}^{B_{\text{lat}}} \sum_{w=1}^{B_{\text{dep}}} d^2_{uvw}(\mathbf{x})}. \tag{2.12}$$

It can be seen that when $\mathbf{x} \in R_{ijk}$, the closer (more away) $\mathbf{x}$ is to the boundary of R_{ijk}, the smaller (larger) the weight $\omega_{ijk}(\mathbf{x})$ is. When $\mathbf{x}$ does not fall within R_{ijk}, $\omega_{ijk}(\mathbf{x})$ is 0. Thus, the final interpolated value at $\mathbf{x}$ depends only on those interpolation functions corresponding to those sub-cuboids that contain $\mathbf{x}$. The idea of making the sub-cuboids overlapping is to maintain smoothness around the boundaries. Furthermore, squaring $d_{ijk}(\mathbf{x})$ in the weight $\omega_{ijk}(\mathbf{x})$ also helps maintain smoothness of the interpolation function.

The blocking strategy effectively reduces computation time of the interpolation method. The computational complexity of the full TPS depends on solving the linear system (2.4), which is $\mathcal{O}(n^3)$. If there are roughly n/B observations in each block, the computational complexity of the blocking scheme is $B(n/B)^3 = B^{-2}n^3$, implying a factor of $1/B^2$ less computation relative to the full sample approach. Algorithm 1 in electronic supplementary material provides the three-dimensional blocking interpolation algorithm. It is noted that the blocking algorithm can be applied to other spatial interpolation methods, for instance, IDW and Kriging.

3. Glider path design

We consider how to efficiently allocate the glider travel paths within the study region so that the collected data yield a more accurate reconstruction of the hydrographic field of the eddy. In this study, the glider paths are 'line segments' [23,54] when viewed vertically from above with repeated diving to a specified depth and climbing to the sea surface following straight line segments; see figure 3 for illustration. This is consistent with the commonly adopted path patterns for gliders [30,55]. As the purpose of the glider path design is for the reconstruction of the three-dimensional hydrographic field of the mesoscale eddy, we aim to find a line-segment pattern that minimizes reconstruction error based on data collected along the designated paths.

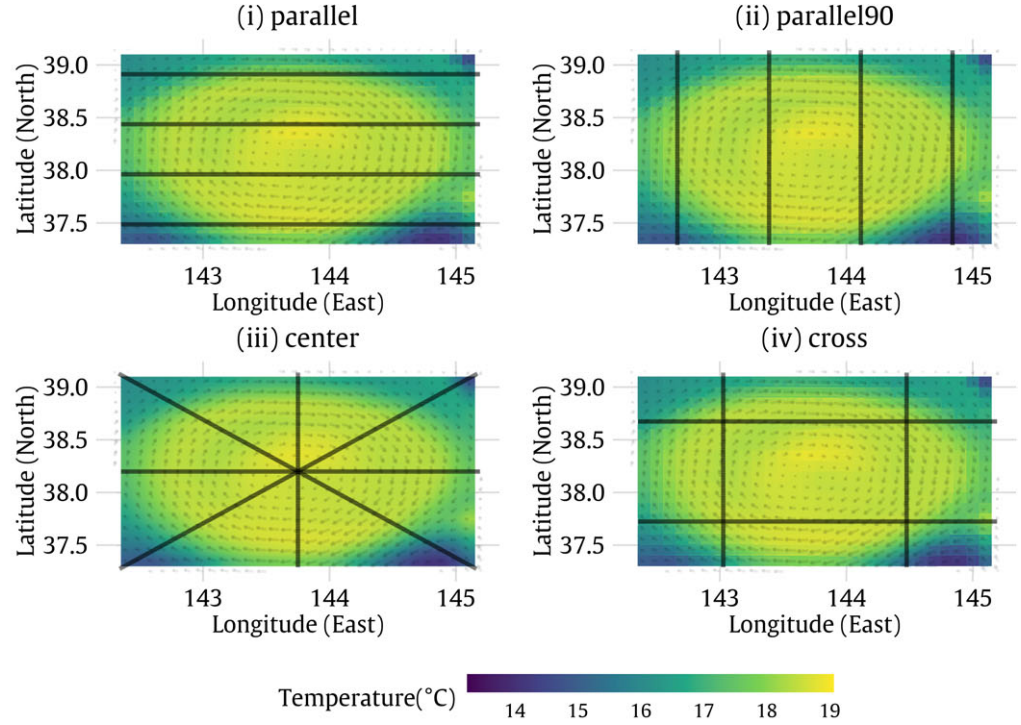

(a) Different glider pathways for 4 gliders

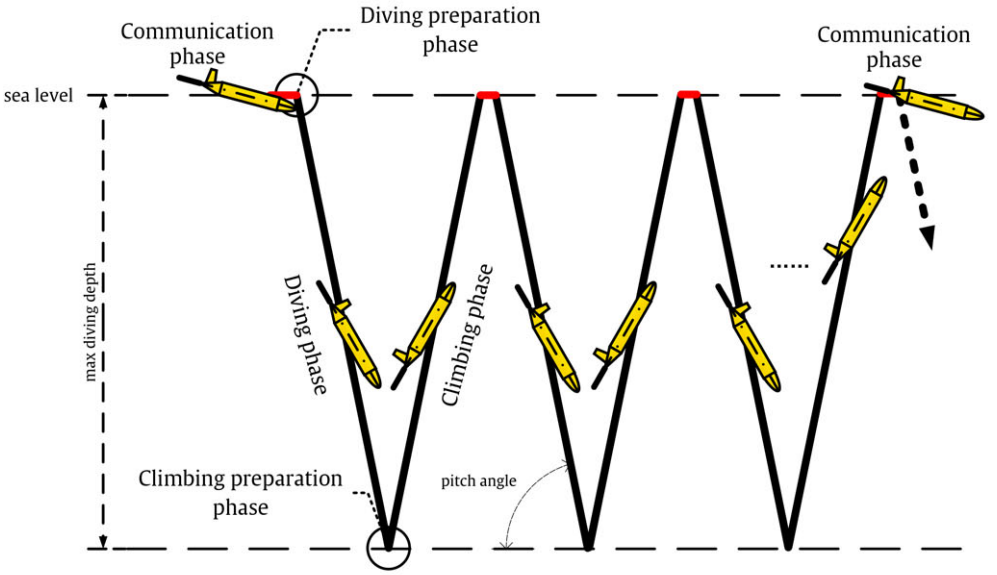

(b) Repeated diving and climbing motions of the underwater glider

Figure 3. (a) The projection of the underwater gliders' trajectory on the sea level (four different path designs) and (b) its diving and climbing motions on the vertical section.

Suppose there are K gliders and a set of glider path formations denoted as $\{\mathcal{A}_j\}_{j=1}^{M}$ at our disposal. Figure 3 presents four examples of path formations for $K = 4$ gliders:

— Parallel: K parallel lines passing through the eddy in the zonal direction;

— Parallel90: K parallel lines passing through the eddy in the meridional direction;
— Centre: K lines all passing through the estimated eddy centre with equal rotation angles;
— Cross: Two sets (each having $K/2$ gliders) of parallel lines, which are mutually perpendicular.

The cross formation above applies to even K and can be extended to odd K with near half splitting of the horizontal and vertical sets. In this study, we focus on linear path designs, which are practical and easy to implement in field deployments. Other nonlinear trajectories, such as circular or spiral paths, may be incorporated through polar coordinate transformations. We restrict our analysis to four representative linear configurations for simplicity.

The purpose of the path design is to find the best path formation with the minimum reconstruction error among the candidate formations $\{\mathcal{A}_j\}_{j=1}^M$ based on a training dataset. The training dataset can be obtained from satellite remote sensing measurements regarding an eddy's SST, sea surface salinity (SSS), or SSH, using sources such as Operational Sea Surface Temperature and Ice Analysis (OSTIA) for SST [56], SMOS for SSS [57] and Archiving, Validation and Interpretation of Satellite Oceanographic Data (AVISO) for SSH [58]. Although these estimates are subject to estimation errors, particularly since eddy signatures in satellite-derived salinity are often weak, they remain highly stable and available in near-real time [59]. These measurements may be augmented by ocean circulation models, which can provide estimate of three-dimensional hydrographic fields by combining observations via data assimilation [60,61]. A state-of-the-art ocean reanalysis data product is GLORYS developed by Mercator Ocean International. Together, these data provide valuable information on the overall structure of the temperature and salinity fields of the eddy and can be used to guide glider path design. In the empirical study reported later, we use training data generated from a high-resolution Community Earth System Model (CESM [62]) with an oceanic resolution of 10km. The CESM output, derived purely from numerical simulation, served as an idealized dataset to establish a framework for glider path design. To assess real-world applicability, we tested our approach on three eddies in the Kuroshio extension region using the GLORYS analysis product in §7. GLORYS matched observed eddies more closely than CESM and thus was used as validation data to evaluate the robustness of the proposed method under realistic conditions.

The data collection by the gliders is determined not only by the sampling path, but also by factors such as glider speed, maximum diving depth, pitch angle and sampling interval. We treat these latter factors as given in the path design.

For a glider path formation $\mathcal{A}_j$, the K gliders collect information such as the temperature or salinity Y_i at locations $\mathbf{X}_i = (X_{i,1}, X_{i,2}, X_{i,3})$ for $i = 1, 2, \ldots, n$ along the line paths. Then we use the sampled data $\{(X_i, Y_i)\}_{i=1}^n$ to fit an interpolation function $\hat{f}_j^*(\mathbf{x})$, and evaluate the interpolation error on a test data set $\mathcal{T} = \{(\mathbf{Z}_1, T_1), \ldots, (\mathbf{Z}_N, T_N)\}$. The reconstruction root-mean-square error (RMSE) is given by

$$\mathrm{RMSE}(\mathcal{A}_j) = \sqrt{\frac{1}{N}\sum_{t=1}^{N}(\hat{f}_j^*(\mathbf{Z}_t) - T_t)^2}. \tag{3.1}$$

Glider path design is to find a design $\mathcal{A}^*$ among the candidate set $\{\mathcal{A}_j\}_{j=1}^M$, which minimizes the reconstruction RMSE among all formations designs $\{\mathcal{A}_j\}_{j=1}^M$, namely,

$$\mathcal{A}^* = \underset{j=1,2,\ldots,m}{\operatorname{argmin}}\ \mathrm{RMSE}(\mathcal{A}_j). \tag{3.2}$$

While glider path design had been studied from various perspectives, such as minimizing two-dimensional surface reconstruction errors [35] and optimizing energy consumption [63], approaches which explicitly aim to minimize three-dimensional hydrographic field reconstruction error are rare. Our design framework focuses on reconstruction accuracy.

4. Methods for glider path control

In this section, we present an adaptive path control algorithm to make the gliders follow the designed pathways in the presence of ocean currents. The path control faces two challenges. One is that glider's position is known only when it surfaces for GPS signals, and the other is that ocean currents can disturb its travel along the designed trajectory. We conduct path control by adjusting the glider's heading angle at each surfacing, based on its position, the available current data and the pre-planned path.

The PID controller is a popular method for dynamic system control. A PID controller continuously calculates the difference $e(t)$ between the target and current positions of the object to be controlled after each time t, and applies corrections based on the proportional (P), integral (I) and derivative (D) of $e(t)$. The overall control function is

$$u(t) = K_P e(t) + K_I \int_0^t e(s)\,\mathrm{d}s + K_D \frac{\mathrm{d}e(t)}{\mathrm{d}t}, \tag{4.1}$$

where K_P, K_I and K_D are non-negative coefficients. In the case of gliders, $u(t)$ will be used to correct for the heading angle. Sang *et al.* [38] proposed an adaptive fuzzy incremental PID control to dynamically adjust the heading angles; see also [64] for a similar approach. As the PID algorithm is weak against disturbances, it may not work well under strong ocean current [65]. In addition to PID, some studies have used optimization methods for glider path control [40,41]. However, as mentioned in §1, these studies formulated the glider path control problem as a shortest path problem.

For the task of mesoscale eddy reconstruction, we want the gliders to travel along the designed paths unless ocean currents are too strong to make it impossible. We present an optimization framework for glider path control that adjusts the heading angle after each surfacing, using available ocean current information. The ocean current information in practice can be obtained from multiple operational and emerging data sources. For near-real-time observational data, the surface geostrophic velocities derived from satellite altimetry products (e.g. AVISO) serve as a primary input [58]. Furthermore, operational ocean forecasting systems, such as the Mercator Ocean's GLO12, provide predictive current fields and AI-based forecast models have also shown considerable promise in providing accurate and computationally efficient predictions [66].

Considering that we can interact with the glider only when it surfaces, and the glider path design is largely two-dimensional in terms of sea surface plane, we represent the path control as a two-dimensional problem ignoring depth. Suppose that the starting and destination positions of a designed line path are, respectively, $\boldsymbol{x}_{\text{start}} = (x_{\text{start},1}, x_{\text{start},2})$ and $\boldsymbol{x}_{\text{target}} = (x_{\text{target},1}, x_{\text{target},2})$ on the sea surface. We assume that the parameters such as glider's speed, the pitch angle and the maximum dive depth remain fixed throughout the mission. Therefore, the control variable is the turning (or heading) angle. Specifically, each time the glider surfaces and waits for instructions for its next move, we determine and adjust the turning angle α to adjust its direction for the subsequent path segment (dive).

Let $\boldsymbol{x}_i$ be the position on the sea surface of the glider after ith diving and climbing motions. At each $\boldsymbol{x}_i$, we want to decide the next turning angle α_{i+1}. Then, one has to consider what control strategy is optimal for the next H diving and climbing motions, rather than just for one step ahead. The next H positions of glider $\{\boldsymbol{x}_{i+1}, \ldots, \boldsymbol{x}_{i+H}\}$ depend on the turning angles $\alpha_{i+1}, \ldots, \alpha_{i+H}$.

To find the best turning angles, we define the objective function as follows. First, we want the realized glider path to follow the designed pathway with the method proposed in §3. A measure of the fidelity of the realized and the designed paths is the average deviation between the H surfacing positions $\{\boldsymbol{x}_{i+l}\}_{l=1}^{H}$ and the designed path line denoted as $\ell : Ax_1 + Bx_2 + C = 0$, where A, B and C are the coefficients defining the straight line connecting the starting position $\boldsymbol{x}_{\text{start}}$ and the destination position $\boldsymbol{x}_{\text{target}}$. This leads to the first part of the objective function:

$$g_1(\alpha_{i+1}, \ldots, \alpha_{i+H}) = \frac{1}{H} \sum_{j=i+1}^{i+H} \frac{|Ax_{j,1} + Bx_{j,2} + C|}{\sqrt{A^2 + B^2}}. \tag{4.2}$$

Minimizing $g_1(\alpha_{i+1},\ldots,\alpha_{i+H})$ would ensure the travel pathway is close to the designed path; however, in a strong current, the glider may get stuck in one place or be blown away from the survey area. This suggests we have to find a compromise between the fidelity to the designed pathway and the overall objective to reach the final destination. To this end, we construct the second objective function

$$g_2(\alpha_{i+1},\ldots,\alpha_{i+H}) = \|\boldsymbol{x}_{\text{target}} - \boldsymbol{x}_{i+H}\|_2. \tag{4.3}$$

Minimizing this objective function drives the glider's position after H steps to be as close as possible to the destination point $\boldsymbol{x}_{\text{target}}$. The overall objective function is a weighted sum of the two:

$$g(\alpha_{i+1},\ldots,\alpha_{i+H}) = w_1 g_1(\alpha_{i+1},\ldots,\alpha_{i+H}) + w_2 g_2(\alpha_{i+1},\ldots,\alpha_{i+H}), \tag{4.4}$$

where the weights w_1 and w_2 depend on ocean current conditions. Generally speaking, if the ocean current is weak (strong), we should make w_1 larger (smaller). Detailed instructions will be given shortly.

Note that although solving (4.4) at $\boldsymbol{x}_i$ yields $(\hat{\alpha}_{i+1},\ldots,\hat{\alpha}_{i+H})$, we apply only $\hat{\alpha}_{i+1}$ to adjust the heading. At the next surfacing, we resolve the H-step optimization again and only use the next immediate heading angle for the immediate next dive. We do not optimize (4.4) over the entire path at once because ocean current forecasts have increasing uncertainty over longer time horizons. Using a relatively small H (we chose $H = 10$) limits the optimization to the range where current predictions have higher reliability, thereby improving the robustness of the resulting path design. Figure 4 displays the algorithmic framework for the main steps in the glider path control problem.

Minimizing (4.4) is a derivative-free optimization problem, so we must use a heuristic algorithm (e.g. DE as in Section S2 in electronic supplementary material) to solve it. To reduce the search space, we limit the turning angle to a range $[-100^\circ, 100^\circ]$ in the implementation and fix $H = 10$. The latter can change according to the ocean current condition or if the glider is near its destination.

The weights in (4.4) are updated each time when the glider surfaces. Let $\boldsymbol{x}_{k-1}$ and $\boldsymbol{x}_k$ denote the glider's positions at the $(k-1)$th and kth surfacings, respectively, let

$$r_{k-1} = \frac{\|\boldsymbol{x}_{k-1} - \boldsymbol{x}_{\text{target}}\|}{\|\boldsymbol{x}_{\text{start}} - \boldsymbol{x}_{\text{target}}\|} \quad \text{and} \quad r_k = \frac{\|\boldsymbol{x}_k - \boldsymbol{x}_{\text{target}}\|}{\|\boldsymbol{x}_{\text{start}} - \boldsymbol{x}_{\text{target}}\|} \tag{4.5}$$

be the relative distance of the two locations to the destination, respectively. Then let

$$\Delta r_k = \max(r_{k-1} - r_k, \varepsilon), \tag{4.6}$$

where $r_{k-1} - r_k$ is the relative distance reduction to the destination and ε is a small positive number, for instance 10^{-5}, to prevent Δr_k from being negative. If Δr_k is close to ε, the glider would have made little progress, and we would decrease w_1 and increase w_2 to make going to the destination a priority for this step. Conversely, if Δr_k is large, then this indicates the glider is progressing well, and we could increase w_1 and decrease w_2 to make following the designed path as a priority.

Next, we discuss how to update w_1 and w_2. First, define $c_k = \delta/\Delta r_k$, where δ is a tuning parameter that reflects the average relative travel distance per diving cycle. The expected number of diving and climbing cycles under static current field is $L\tan\beta/2h$, where L is the length of the designed glider path, h is the diving depth and β is the pitch angle. These mean that the relative distance travelled per diving cycle is $2h/L\tan\beta$. However, considering the presence of ocean current, one may choose $\delta = h/L\tan\beta$. Now the weights are updated according to the following equation:

$$w_{1,k+1} = c_k^{-1} w_{1,k} \quad \text{and} \quad w_{2,k+1} = c_k w_{2,k}. \tag{4.7}$$

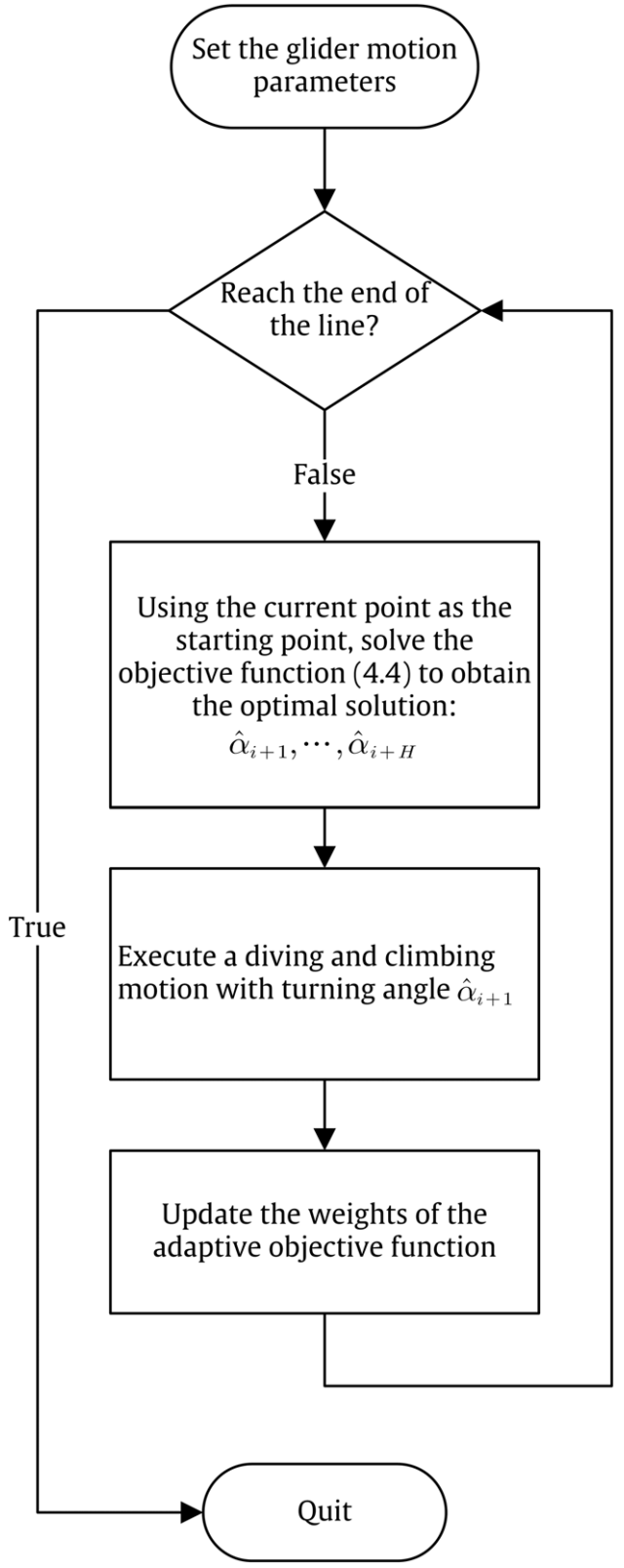

Figure 4. Flowchart of glider path control, where the optimization problem solves the adaptive objective function (4.4).

Algorithm 1: Adaptive glider path control.

Input: $\boldsymbol{x}_{\text{start}}, \boldsymbol{x}_{\text{target}}$, glider initial position $\boldsymbol{x}_0$, the dimension of search space H_0, endpoint tolerance η, and several parameters in adaptive adjustment: $c_{\min}, c_{\max}, w_{1,\min}, w_{1,\max}, w_{2,\min}, w_{2,\max}, \varepsilon, \delta$.

Initialize the heading angle ϕ_0 toward $\boldsymbol{x}_{\text{target}}$;

Initialize weights:

$$w_{1,1} \leftarrow \frac{w_{1,\min} + w_{1,\max}}{2}, w_{2,1} \leftarrow \frac{w_{2,\min} + w_{2,\max}}{2};$$

Initialize search dimension $H \leftarrow H_0$;

$k \leftarrow 1$;

while *the glider is still in the study area or has not exceeded its maximum sailing time* **do**

  Given $(\boldsymbol{x}_{\text{start}}, \boldsymbol{x}_{\text{target}})$, and the position of glider $\boldsymbol{x}_{k-1}$, use heuristic algorithm (e.g. DE) to solve the following optimization problem:

$$\left(\hat{\alpha}_k, \cdots, \hat{\alpha}_{k+H-1}\right)^T \leftarrow \underset{-100^\circ \le \alpha_i \le 100^\circ}{\arg\min} \; w_{1,k} g_1 + w_{2,k} g_2.$$

  Update the heading angle $\phi_k \leftarrow \phi_{k-1} + \hat{\alpha}_k$ and use it for the next diving and climbing motion;

  Gets the current surface position $\boldsymbol{x}_k$ of the glider;

  if $\|\boldsymbol{x}_k - \boldsymbol{x}_{target}\| \le \eta$ **then**

    Break;

  Calculate $r_{k-1} \leftarrow \frac{\|\boldsymbol{x}_{k-1} - \boldsymbol{x}_{\text{target}}\|}{\|\boldsymbol{x}_{\text{start}} - \boldsymbol{x}_{\text{target}}\|}, r_k \leftarrow \frac{\|\boldsymbol{x}_k - \boldsymbol{x}_{\text{target}}\|}{\|\boldsymbol{x}_{\text{start}} - \boldsymbol{x}_{\text{target}}\|}$;

  $\Delta r_k \leftarrow \max\left(r_{k-1} - r_k, \varepsilon\right)$;

  $c_k \leftarrow \max\left\{c_{\min}, \min\left\{\frac{\delta}{\Delta r_k}, c_{\max}\right\}\right\}$;

  Update weights:

$$w_{1,k+1} \leftarrow \max\left\{w_{1,\min}, \min\left\{c_k^{-1} w_{1,k}, w_{1,\max}\right\}\right\},$$

$$w_{2,k+1} \leftarrow \max\left\{w_{2,\min}, \min\left\{c_k w_{2,k}, w_{2,\max}\right\}\right\}.$$

  if $w_{2,k+1} = w_{2,\max}$ **then**

    $H \leftarrow H + H_0$;

  else

    $H \leftarrow \max\{H_0, H - H_0\}$;

  $H \leftarrow \min\left\{H, \lceil \frac{r_k}{\Delta r_k} \rceil\right\}$;

  $k \leftarrow k + 1$;

We bound the update factor c_k to prevent overly drastic weight changes. Specifically, we set

$$c_k^* = \begin{cases} c_{\min}, & \text{if } c_k \le c_{\min}, \\ c_k, & \text{if } c_{\min} < c_k \le c_{\max}, \\ c_{\max}, & \text{if } c_k > c_{\max}. \end{cases} \tag{4.8}$$

One may set $c_{\min}$ and $c_{\max}$ to be the reciprocal of each other, for instance, $c_{\min} = 0.1$ and $c_{\max} = 10$. We also introduce $w_{1,\min}, w_{1,\max}$ and $w_{2,\min}, w_{2,\max}$ to restrain w_1 and w_2 from both ends, respectively, to prevent one of the objective functions from being too dominant. Without such bounds, the weights could become excessively large or small under certain ocean conditions. Algorithm 1 outlines the algorithm for the adaptive glider path control.

Considering that the velocity field of the ocean current is only available for the surface, one has to estimate the current field beneath the surface, which can be made via the ocean models or the historical data by establishing the relationship between the ocean surface current and the ocean

interior current. The estimation of subsurface currents from surface information will be discussed in §6a.

5. Experimental results for path design

This section reports results from numerical evaluation of the proposed procedure based on a simulated mesoscale eddy from CESM on 18 March 1989 over a region with latitude 37.25°N–39.15°N and longitude 142.3°E–145.2°E. The spatial resolution of the simulated mesoscale eddy was $0.1^\circ \times 0.1^\circ$, and there were 39 levels from the sea surface to 830 m below, which makes $30 \times 20 \times 39 = 23\,400$ grid boxes in the three-dimensional space for the eddy.

By treating the simulated eddy as the ground truth, we focused on the reconstruction accuracy of its temperature and salinity fields. The aim of the path design experiment was to determine how many gliders and what path formation yielded accurate reconstructions in the absence of any currents. This can be viewed as designing for an eddy's hydrographic field at a time, while the design can be updated when the hydrographic field information is updated. This is why we propose the blocking method for the TPS for more rapid computation and design. In practice, the hydrographic field may be obtained from a real-time numerical model or data assimilation system [60,67], like CESM or GLORYS. We have also applied our approach to three Kuroshio extension eddies with reanalysis data from GLORYS to demonstrate its applicability to time-evolving eddies in §7 and the electronic supplementary material.

In the simulation, we used the Petrel-II underwater glider as the reference platform [55,68]. Specifically, we set the pitch angle to 20°, the sampling interval to 50 s, the horizontal velocity to $0.5\,\mathrm{m\,s^{-1}}$ and the vertical velocity to $0.2\,\mathrm{m\,s^{-1}}$, with a maximum diving depth of 800 m. These parameter values were quite general and fell well within the standard operational envelope of modern gliders [69].

(a) Comparing different interpolation methods

Before evaluating the effectiveness of the proposed glider path design and control, we first compare the performance of three interpolation methods: the IDW, the Kriging and the TPS interpolations. In addition, we tried two blocking strategies. One had three-dimensional overlapping blocks as described in Algorithm 1, electronic supplementary material, where we set $B_{\mathrm{long}} = 3$, $B_{\mathrm{lat}} = 2$ and $B_{\mathrm{dep}} = 4$ with a block overlapping ratio $c = 0.25$; and on the other hand, the blocks confined in the two-dimensional plane at a given depth, namely, the two-dimensional interpolation was performed on each of the 39 depths. For the IDW interpolation, we set the power parameter $p = 5$ for both the three- and two-dimensional blockings according to the cross-validation results. The smoothing parameter λ used by the TPS was obtained by minimizing the GCV score [34,70]. The Kriging interpolation was implemented using MATLAB's fitgpr function, with the default Gaussian kernel, and the parameters of the kernel function were determined using the built-in cross-validation method.

Table 1 presents the RMSEs from the five-fold cross-validation where the $30 \times 20 \times 39 = 23\,400$ grids eddy data were randomly partitioned to five portions with four portions being used to train the interpolation model, while the remaining portion for calculating the prediction RMSEs. This cross-validation operation was repeated five times to obtain the cross-validated RMSEs for the three interpolation methods coupled with the two blocking schemes. Using two-dimensional blocking, the Kriging method achieved the lowest RMSEs, followed by the IDW and the TPS. The reason for the poor performance of the TPS with the two-dimensional blocking was that the temperature and the salinity field of the eddy have strong vertical dependence as shown in figure 1, and the TPS interpolation tends to give smoother estimates than the other two methods, while the slices of plane blocks remove much of the vertical dependence. However, when the vertical dependence was included in the three-dimensional blocking scheme, the TPS interpolation exhibited its advantage over the other two methods. Indeed, the block TPS interpolation attained the smallest RMSEs in both the temperature and salinity reconstruction

Table 1. Root-mean-square errors based on the five-fold cross-validation. ($RMSE_{CV}$) of the reconstructed eddy hydrographic field using three interpolation methods: the IDW, the Kriging and the proposed thin plate spline (TPS) with the two blocking schemes: the two- and three-dimensional blocking schemes.

	$RMSE_{CV}$	
Method	Temperature (°C)	Salinity (psu)
IDW.2D	0.265	0.0533
IDW.3D	0.215	0.0450
Kriging.2D	0.131	0.0262
Kriging.3D	0.113	0.0238
TPS.2D	0.307	0.0642
TPS.3D	**0.103**	**0.0203**

among all settings. The three-dimensional TPS had 9.3% and 14.5% lower RMSEs for temperature and salinity reconstruction, respectively, than those of the Kriging, and far lower than those of the IDW. Thus, in the rest of the simulation, only the three-dimensional TPS interpolation was considered.

(b) Path design

We compare reconstruction performance with respect to different path designs and different numbers of gliders. The path design with four gliders is shown in figure 3a. Four to ten gliders were used in the simulation experiments using the design procedure described in §3.

Section 2b has discussed the computation time with respect to the number of blocks. Figure 3a that the glider's sample coverage in the latitude and longitude plane was quite sparse in remote areas from the allocated glider paths. Hence, the number of blocks with respect to the longitude and latitude should not be too large, and we set $B_{\text{long}} = B_{\text{lat}} = 3$. Given that the glider's Conductivity-Temperature-Depth (CTD) sensor can sample at high frequency, there is effectively no extra sparsity with respect to depth. Therefore, we choose the number of blocks in the vertical direction ranging from 10, 20, 40, to 80 in the simulation experiments.

Table 2 summarizes the reconstruction RMSEs of the eddy temperature and salinity fields, the glider sampling effort in travel length and the correlation between the TPS interpolations and the actual values of the underlying eddy field, with respect to varying numbers of gliders. It also presents results with respect to the number of vertical layer blocks B_{dep} and different path design patterns.

Tables 2(a) and (b) show that as the number of gliders increased, the reconstruction RMSEs decreased nearly monotonically for each given pattern of path designs. The Parallel and the Centre designs yielded the lowest RMSEs among the four patterns for temperature, and the centre design had the lowest RMSE for salinity. Notably, the Centre design required the longest travel distance, whereas the Parallel90 design required the smallest. Despite more effort, the Centre design did not always achieve the lowest temperature RMSE nor did Parallel90 consistently produce the best results. The cross design generally had higher RMSEs than the Parallel90 design despite having travelled longer distance. Additionally, for the four-glider centre case, the TPS system matrix in (2.4) became singular, so no reconstruction result could be obtained for that scenario.

The reason for the Centre design having the lowest reconstruction RMSEs for salinity for all numbers of gliders considered, while it was not always the best for temperature reconstruction, was that the structure of the underlying salinity field was more circular shaped than that of the temperature field as shown in figure 1, especially in the shallow depth. It is noted that the centre design had been commonly employed in ocean glider surveys.

Table 2. (a) RMSE for reconstructed temperature (°C) fields in panel (a) and for Salinity (psu) field in panel (b), along with the correlation coefficient (Corr.) with their respective true values for different path designs with respect to different number of gliders and the length of the designated paths (in km). Panel (c) presents the temperature (°C) field reconstruction RMSE and CPU time with respect to different number of blocks.

	glider path design											
	Parallel			Parallel90			Centre			Cross		
number of gliders	length	RMSE	Corr.	length	RMSE	Corr.	length	RMSE	Corr.	length	RMSE	Corr.
(a) Temperature field reconstruction performance with $B_{long} = B_{lat} = 3$ and $B_{dep} = 40$												
4	1027	0.383	0.9979	845	**0.364**	**0.9981**	1449	/	/	936	0.613	0.9945
5	1283	**0.244**	**0.9991**	1056	0.279	0.9989	1449	0.289	0.9988	1193	0.422	0.9974
6	1540	0.196	0.9994	1268	0.225	0.9992	1872	**0.188**	**0.9995**	1404	0.313	0.9986
7	1797	**0.134**	**0.9997**	1479	0.164	0.9996	1872	0.167	0.9996	1661	0.209	0.9994
8	2053	0.112	0.9998	1690	0.132	0.9997	2385	**0.101**	**0.9999**	1872	0.158	0.9996
9	2310	0.095	**0.9999**	1901	0.112	0.9998	2385	**0.091**	**0.9999**	2128	0.118	0.9998
10	2567	**0.072**	**0.9999**	2113	0.088	**0.9999**	2808	0.082	**0.9999**	2340	0.094	**0.9999**
(b) Salinity field reconstruction performance with $B_{long} = B_{lat} = 3$ and $B_{dep} = 40$												
4	1027	0.0568	0.9645	845	**0.0529**	**0.9692**	1449	/	/	936	0.0678	0.9494
5	1283	0.0411	0.9816	1056	0.0423	0.9803	1449	**0.0366**	**0.9857**	1193	0.0574	0.9662
6	1540	0.0338	0.9876	1268	0.0339	0.9874	1872	**0.0279**	**0.9915**	1404	0.0461	0.9771
7	1797	0.0251	0.9933	1479	0.0257	0.9928	1872	**0.0222**	**0.9946**	1661	0.0379	0.9844
8	2053	0.0220	0.9948	1690	0.0214	0.9951	2385	**0.0153**	**0.9975**	1872	0.0310	0.9895
9	2310	0.0189	0.9961	1901	0.0183	0.9964	2385	**0.0146**	**0.9977**	2128	0.0224	0.9945
10	2567	0.0153	0.9975	2113	0.0150	0.9976	2808	**0.0143**	**0.9978**	2340	0.0188	0.9961

(*Continued.*)

Table 2. (*Continued*.)

	B_{dep}, the number of blocks in depth							
	10		20		40		80	
number of gliders	RMSE	time	RMSE	time	RMSE	time	RMSE	time
(c) Temperature field reconstruction under different number of blocks B_{dep} and different number of gliders under 'Parallel' design with $B_{long} = B_{lat} = 3$								
4	0.371	14.76 min	0.376	3.99 min	0.383	1.33 min	0.392	43.63 sec
5	0.233	26.32 min	0.237	7.67 min	0.244	2.26 min	0.252	1.17 min
6	0.184	1.44 hour	0.190	24.41 min	0.196	7.72 min	0.208	3.05 min
7	0.122	1.06 hour	0.128	19.48 min	0.134	5.24 min	0.144	2.21 min
8	0.101	1.91 hour	0.106	34.98 min	0.112	9.30 min	0.119	3.94 min

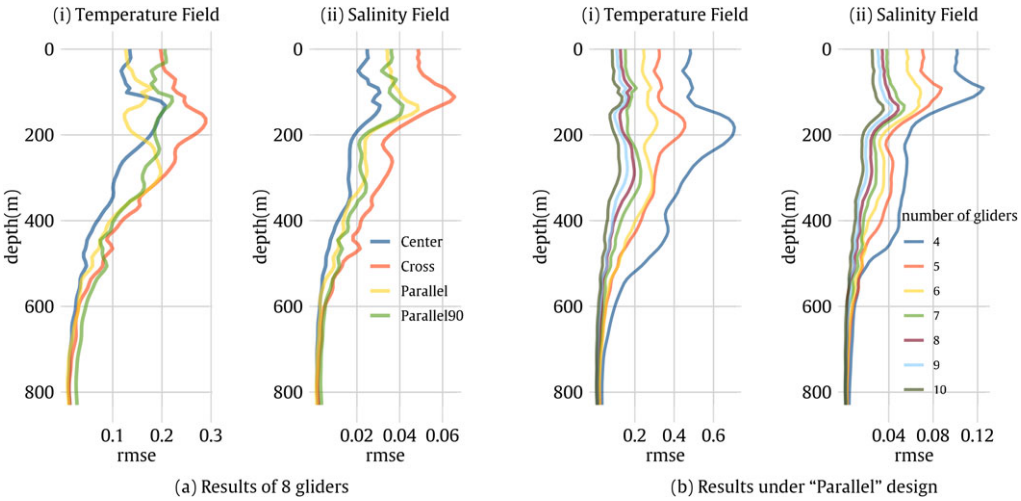

Figure 5. Vertical reconstruction RMSEs with respect to the depth for temperature (°C, left panels) and salinity (psu, right panels) fields for the simulated eddy with (a) different path designs and (b) different number of gliders.

Overall, the difference between the reconstruction RMSEs among the three formations: Centre, Parallel and Parallel90 were not very large with the latter two designs affording smaller effort. From the perspective of practical oceanic implementation, the Parallel and Parallel90 formations offer easier gliders release and recovery logistic than the Centre formation, as well as requiring less glider travel effort. It is noted that for the Centre design, owing to the rectangle shape of the survey area and the equal angle allocation, the total travel distance with $2k$ gliders is the same as that with $2k + 1$ gliders. However, the sample coverage with $2k + 1$ gliders is greater than that of $2k$ gliders, leading to a reduction in reconstruction error.

Table 2(c) shows that when the number of vertical block B_{dep} was increased, the amount of reconstruction time was much reduced with the reduction rate being more than halved when B_{dep} was doubled each time, while the RMSEs were only slightly increased. The increase in the RMSE was small when compared with the substantial amount of computational saving. For the Parallel design, if the number of gliders was increased from 4 to 8, the reconstruction RMSE of the temperature field decreased from 0.3831 to 0.1124, which was only 1/3 of that with four gliders.

Figure 5 displays the reconstruction errors of the hydrographic fields at different depths using different path designs with eight gliders (figure 5a) and varying numbers of gliders under the Parallel design (figure 5b). The vertical distribution of the reconstruction error largely reflected the vertical gradients of the eddy, which becomes less variable as the depth increased. The largest reconstruction error occurred between 100 and 300 m, where the thermocline is located [30]. The Centre design achieved better reconstruction results for both temperature and salinity fields. For the Parallel design, reconstruction errors decreased uniformly across depth as the number of gliders increased. However, when the number of gliders reached 7, the additional benefit of adding more gliders was not significant.

A smaller number of gliders will be considered in an empirical analysis on three real eddies in the Kuroshio extension region in §7 and in the electronic supplementary material. The results with a less number of gliders were generally consistent with those in table 2 and figure 5, demonstrating the robustness and satisfactory performance of the proposed method under different oceanic conditions.

6. Experimental results for path control

In this section, we apply algorithm 1 to five different missions and solve the glider path control sub-problem with several evolutionary algorithms. We used the same simulated eddy with an

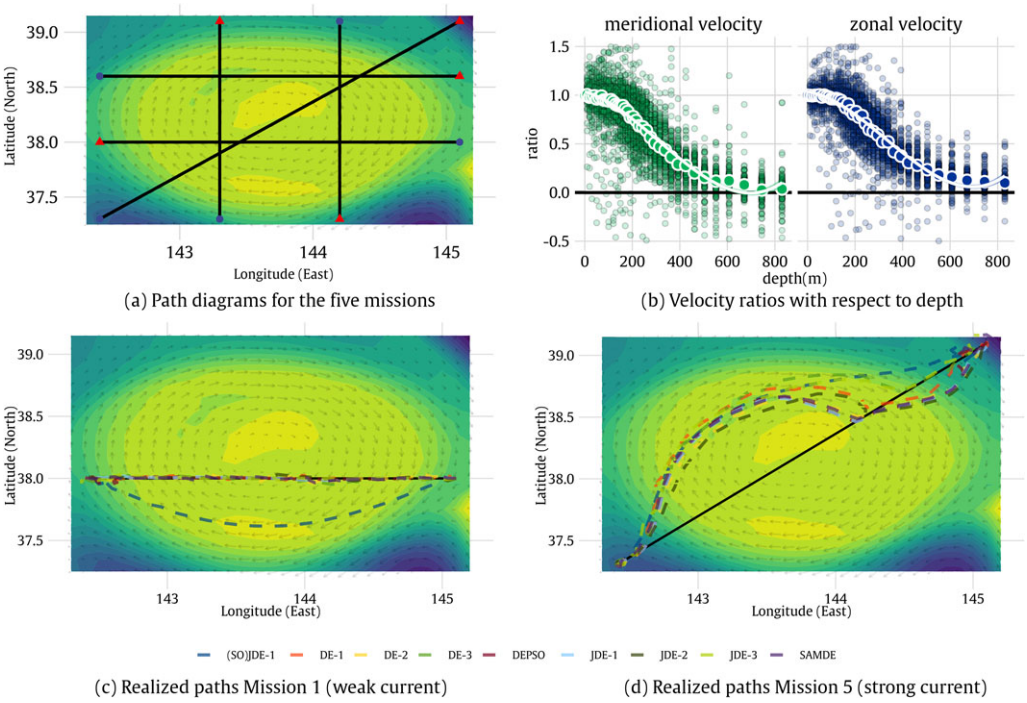

(a) Path diagrams for the five missions

(b) Velocity ratios with respect to depth

(c) Realized paths Mission 1 (weak current)

(d) Realized paths Mission 5 (strong current)

Figure 6. (a) Designed path diagrams for the five missions where the blue dots and red triangles represent the start and end points of the missions, and the arrows represent the ocean current on the sea surface; and (b) scattered plots of randomly selected 5000 velocity ratios (the subsurface velocity relative to the surface velocity at a depth) and ocean depth with the fitted cubic polynomial regression for zonal velocity (left panel) and meridional velocity (right panel) where the average ratios at different depths are marked by bigger circles. (c,d) Realized glider paths for the simulated eddy by solving the glider path control subproblem with different algorithms on Mission 1 (c) and Mission 5 (d), where SO means that the single objective function (4.3) is adopted.

Table 3. Coordinates of the start and end points of the line paths of the five missions

mission ID	start point	end point
1	(145.1°E, 38.0°N)	(142.4°E, 38.0°N)
2	(142.4°E, 38.6°N)	(145.1°E, 38.6°N)
3	(143.3°E, 37.3°N)	(143.3°E, 39.1°N)
4	(144.2°E, 39.1°N)	(144.2°E, 37.3°N)
5	(142.4°E, 37.3°N)	(145.1°E, 39.1°N)

expanded time window (18–28 March 1989) as the ground truth. The starting and ending locations of the five missions are reported in table 3, while their travel paths are shown in Figure 6a. We used the daily-averaged CESM velocity field as the true flow field in the glider simulations. As the simulation time advances day by day, we switch to each day's velocity field to mimic an actual multi-day mission, where only the surface current was assumed to be observable.

We evaluated the following algorithms for the control optimization sub-problem. These included DE and self-adaptive DE (JDE [71]), each implemented with three strategy variants (strategies 1–3; details in electronic supplementary material §S2). Among the three evolution strategies, strategy 1 emphasizes the survival of the fittest, strategy 3 focuses on diversity and strategy 2 is a balance of the strategies 1 and 3. We also tested the self-adaptive multi-population

DE (SAMDE [72]), which is designed to increase population diversity, and a DEPSO algorithm that hybridizes DE with Particle Swarm Optimization (PSO) [73,74]. Compared with DE, PSO is a non-monotonic (more exploratory) search strategy. Combining PSO with DE can greatly increase population diversity. The parameter settings for the DE and JDE algorithms are given in Table S1 in the electronic supplementary material.

(a) Ocean current field imputation

Solving the objective function (4.4) required real-time ocean current data. However, only the surface current can be obtained from satellite remote sensing data [75,76]. Surface current measurements had been considered a useful input for underwater glider control [77]. Several studies suggested that, under certain oceanographic conditions, a dynamical correlation often exists between deep-water currents and surface currents [78,79]. This principle underlies some oceanographic reconstruction techniques, such as the interior-surface quasigeostrophic method [80], which infer subsurface flow fields from surface observations in regions dominated by geostrophic balance. We use a statistical approach that imputes the subsurface ocean current velocity from the surface current measurements as described below. In practice, near-real-time sea surface velocity can be obtained by calculating geostrophic velocity fields from satellite altimetry observations, such as those provided by Global Ocean Gridded L4 Sea Surface Heights [81].

We used the eddy data from CESM over the period from 16 February to 17 March 1989 as the training data to learn the statistical relationship between surface and subsurface ocean current velocities. The learned relationship is then used in the glider path control to impute real-time subsurface velocities when surface velocities are available. As mentioned earlier, near-real-time surface current field is accessible in data products like CESM or GLORYS.

Across the 30-day period and 23 400 grid points in the study region, we obtained a total of 702 000 observations. Let $v_{\text{zon}}(\boldsymbol{x}_k)$, $v_{\text{mer}}(\boldsymbol{x}_k)$ and $v_{\text{ver}}(\boldsymbol{x}_k)$ denote the zonal (eastward), meridional (northward) and vertical (downward) velocity components at a location $\boldsymbol{x}_k = (x_{k1}, x_{k2}, x_{k3})$ for $k = 1, 2, \ldots, 702\,000$. Our initial analysis of the simulated eddy data showed that the vertical velocity component in the target region was on the order of $10^{-4}\,\text{m s}^{-1}$, which was negligible compared to both the vertical velocity of the glider ($0.17\,\text{m s}^{-1}$) and the absolute horizontal eddy velocity ($1.28\,\text{m s}^{-1}$). Therefore, we considered only the two horizontal velocity components, v_{zon} and v_{mer}.

Let $\rho_{\text{zon},k} = v_{\text{zon}}(\boldsymbol{x}_k)/v_{\text{zon}}(x_{k1}, x_{k2}, 0)$ and $\rho_{\text{mer},k} = v_{\text{mer}}(\boldsymbol{x}_k)/v_{\text{mer}}(x_{k1}, x_{k2}, 0)$ be the velocity ratios at depth x_{k3} relative to that at the surface. Figure 6b displays scatter plots of the two ratios and their local averages with respect to the depth x_{k3}, which show some level of nonlinearity. Outliers with ratios greater than 1.5 or less than -0.5 were excluded from the analysis (175 cases for meridional velocity and 74 for zonal velocity). This motivated us to consider a cubic polynomial regression model for the velocity ratio and the depth:

$$\rho_{\text{zon},k} = \beta_{\text{zon},0} + \sum_{i=1}^{3} \beta_{\text{zon},i} x_{k3}^i + \varepsilon_k. \tag{6.1}$$

The coefficients $\{\beta_{\text{zon},i}\}_{i=0}^3$ of the cubic regression (6.1) were estimated using the least squares method. As shown in table 4, the cubic regression provided a fit to the simulated data with statistically significant cubic term and quite high coefficient of determination R^2, indicating its strong explanation power. The corresponding velocity ratios are displayed in figure 6b.

Utilizing the estimated cubic polynomial regression, for an arbitrary location $\boldsymbol{x}_0 = (x_{01}, x_{02}, x_{03})$, given the real-time ocean current velocity $v_{\text{zon}}(x_{01}, x_{02}, 0)$ on the sea surface, the ocean current velocity at $\boldsymbol{x}_0$ with depth x_{03} is imputed as follows:

$$\hat{v}_{\text{zon}}(\boldsymbol{x}_0) = \hat{\rho}_{\text{zon}}(x_{03}) \cdot v_{\text{zon}}(x_{01}, x_{02}, 0), \tag{6.2}$$

Table 4. The results of the cubic polynomial regression of the zonal velocity ratio and meridional velocity ratio with parameter estimates, standard errors (s.e.), *t*-test results, the coefficient of determination (R^2) and the *F*-test results.

direction		estimate	s.e.	*t*-stat	*p*-value	R^2	*F*-stat	*p*-value
zonal	(Intercept)	1.03	3.08×10^{-3}	335.51	0	0.774	2.64×10^{4}	0
	$x_{k,3}$	-3.84×10^{-4}	3.80×10^{-5}	−10.11	5.42×10^{-24}			
	$x_{k,3}^2$	-4.93×10^{-6}	1.20×10^{-7}	−41.19	0			
	$x_{k,3}^3$	4.98×10^{-9}	1.02×10^{-10}	48.85	0			
meridional	(Intercept)	1.03	3.85×10^{-3}	267.00	0	0.711	1.84×10^{4}	0
	$x_{k,3}$	-6.27×10^{-4}	4.75×10^{-5}	−13.21	1.05×10^{-39}			
	$x_{k,3}^2$	-4.62×10^{-6}	1.50×10^{-7}	−30.79	0			
	$x_{k,3}^3$	4.87×10^{-9}	1.28×10^{-10}	38.14	0			

where $\hat{\rho}_{\text{zon}}(x_{03}) = \hat{\beta}_{\text{zon},0} + \sum_{r=1}^{3} \hat{\beta}_{\text{zon},r} x_{03}^r$. The $\hat{v}_{\text{mer}}(\boldsymbol{x}_0)$ can be obtained similarly. These regression equations, which can be used for imputing the current field beneath the ocean surface, were used later in the glider path control experiments.

(b) Path control

Figure 6 displays the realized glider pathways administered by the control algorithms for Missions 1 and 5, which had different travel paths over the same eddy. The pathway of Mission 1 was designed in a region with calmer water and weaker currents, while that of Mission 5 traversed areas with stronger currents and greater current shear, making it the most challenging among the five missions. The results for all missions are reported in Figure S1 in the electronic supplementary material. The effects of the ocean current was clearly reflected in the realized glider paths and their average deviations from the planned pathway in figure 6, which show much larger deviations for Mission 5 owing to its encountering the strongest current among the five missions. The current for Mission 5 was so strong that all the paths directed by the algorithms were 'blown away' from the designated path for a substantial amount of time. However, as the proposed procedure has a built-in component to counter the strong current by increasing weight w_2 to the distance to the final destination, the gliders all withstood the strong current and managed to finish the mission without being stuck or lost altogether.

Figure 7 reports the minimum, maximum and average deviations to the designed paths of the eight algorithms based on 10 replications, with the algorithms being ranked from bottom up according to their average deviation. It is observed that the three deviation measures were highly correlated. Figure 7e reports the ranks of the algorithms based on the average deviations, which shows that DEPSO was the best performing algorithm, being the best for two missions and among the top three for the other three missions. JDE-2 was the second best, being the best for one mission and always in the top four, while JDE-1 was the best for the most difficult Mission 5. It appears that the JDE algorithms were better performing than the DE variants. In particular, DEPSO, JDE-1 and JDE-2 occupied the top three spots in terms of the average deviations, while SAMDE ranked the fourth. As reported in Table S2 in electronic supplementary material, SAMDE used the least amount of computing time with the average time spent for the optimization per gilder surfacing was 13.2 s. The average computation time was generally no more than 30 s, which was acceptable in the dynamic path control problem. For the best performing DEPSO and JDE-2, the average computing time was 21.2 s and 18.5 s, respectively. These would be acceptable for real field control missions. More aspects of the results are reported in Section S3 in the electronic supplementary material.

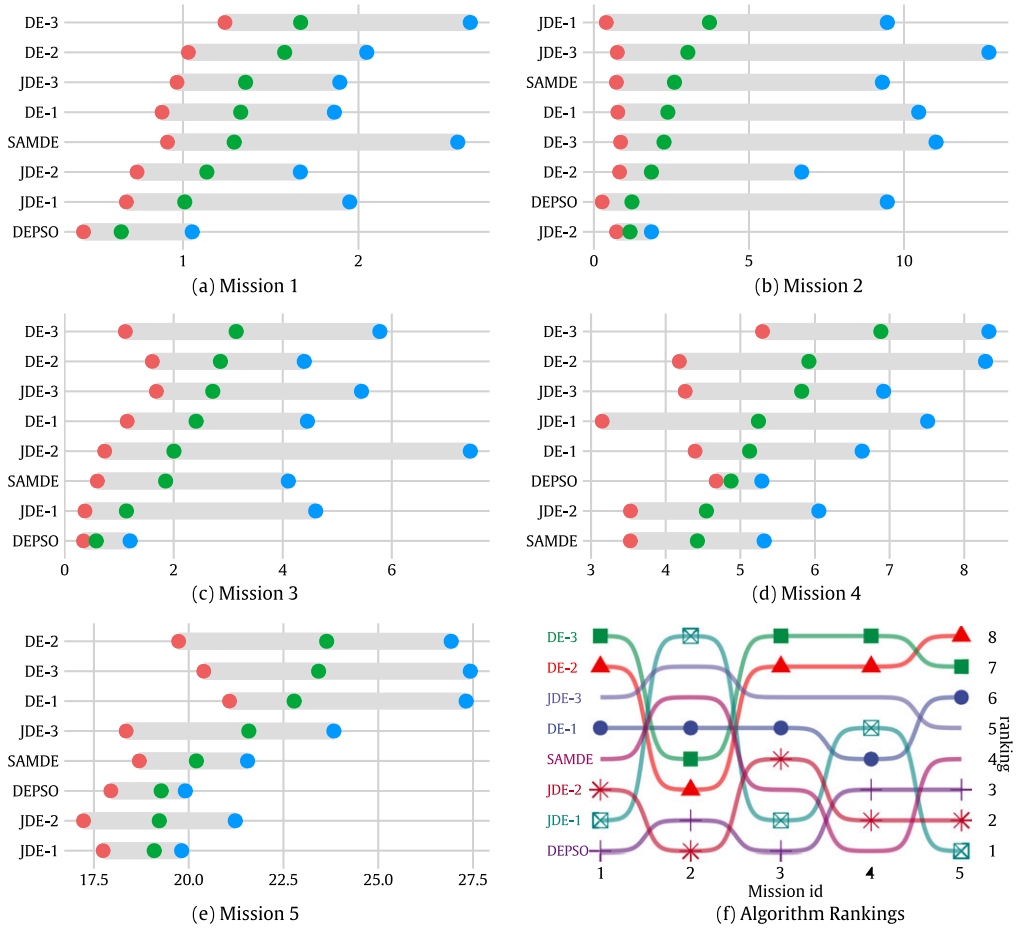

Figure 7. The minimum, average and maximum deviations (in kilometres) of the realized paths by the eight algorithms for Missions 1–5 based on 10 replications (a–e) for the simulated eddy, where red (blue) circles marked the minimums (maximum), and greens were for the averages; (f) rankings of the algorithms for the 5 missions.

7. Validation using real-world eddy data

Having demonstrated the efficacy of the proposed methods on a simulated eddy in the last two sections, we consider experimenting the proposed methods on real eddies. We want to assess the performance of the proposed framework under realistic oceanographic conditions, which include complex background flows and data noise that may not be fully captured in numerically simulated eddies.

We selected three eddies in the Kuroshio extension in August 2024 as shown in Figure S2 in the electronic supplementary material, which consisted of two cyclonic eddies and one anticyclonic eddy. We present here results for a cyclonic eddy ('Eddy 1'), while the results for the other two eddies (Eddy 2 and Eddy 3) are reported in Section S4 in the electronic supplementary material.

We used the GLORYS reanalysis data as the pseudo truth in the evaluation of the reconstruction performance of Eddy 1. Eddy 1's three-dimensional temperature field was reconstructed using different numbers of gliders with four deployment designs. Figure 8 reports the temperature reconstructions accuracy with one to four gliders at the surface and two subsurface depths under the Centre design. It shows that using a single glider was insufficient for the mesoscale eddy reconstruction, as it could not resolve the eddy's spatial variability because of its very limited coverage. The reconstruction accuracy improved with two or three gliders, as their trajectories intersected the eddy centre and provided representative coverage of the eddy's core

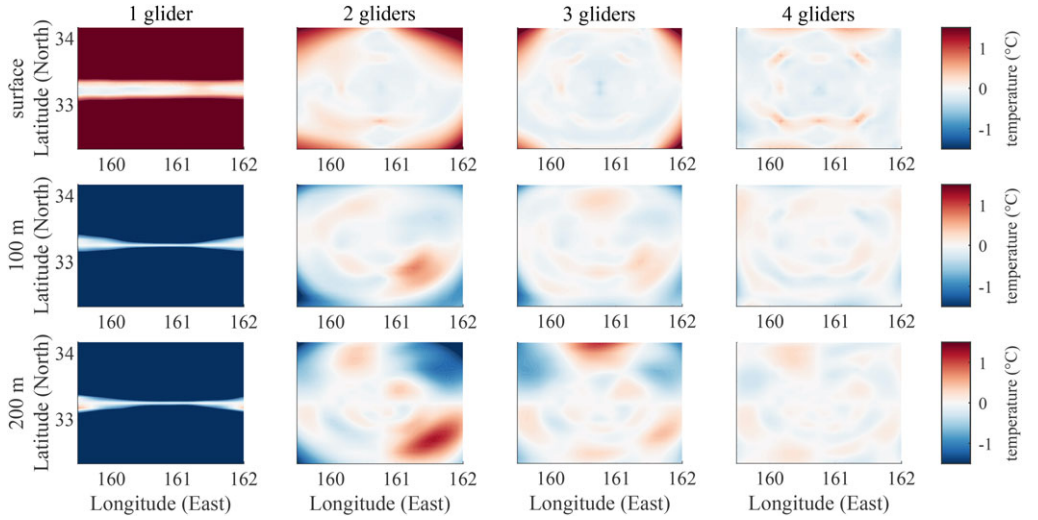

Figure 8. Reconstruction errors under the Centre scheme using 1, 2, 3 and 4 gliders for temperature field of real Eddy 1 at the surface, 100 m and 200 m depths.

and edge regions. However, the accuracy offered with using two to three gliders was still inferior to that with four gliders at all three levels of the depth, especially for reconstructing subsurface thermocline features.

The error distributions for all path designs are provided in Figures S3–S5 in the electronic supplementary material. Figure S6 in the electronic supplementary material further shows the reconstruction for Eddy 1 of four path designs with deployments of 1–10 gliders. The Centre design achieved the best overall performance, particularly in the upper 300 m, followed by the Parallel design. The analysis also showed that increasing the number of gliders to 7 could substantially improve the reconstruction accuracy. However, the marginal gains diminished for using more than seven gliders, suggesting that seven gliders would be near-optimal for practical deployment.

To evaluate the robustness of different interpolation methods to measurement errors, we generated synthetic observations with controlled noise levels. The observed temperature at each sampling point was modelled as $T(\boldsymbol{x}_i) = T^*(\boldsymbol{x}_i) + \sigma \cdot \varepsilon_i$, $\varepsilon_i \overset{\text{i.i.d.}}{\sim} N(0,1)$, for $i = 1, 2, \ldots, n$, where $T^*(\boldsymbol{x}_i)$ represents the pseudo true temperature from GLORYS reanalysis and σ controls the magnitude of measurement errors. Eddy 1 was then sampled along the glider paths using four, six and eight gliders under the Parallel and Parallel90 schemes, and the resulting observations were used to reconstruct the three-dimensional temperature field with three interpolation methods: the IDW, the Kriging and the TPS. For the Kriging, we employed two widely used semivariogram functions in geosciences, the Gaussian and the Matérn kernels.

Figure S7 in electronic supplementary material summarizes the reconstruction results, which showed that the TPS consistently outperformed the Kriging and the IDW in terms of reconstruction error. Notably, the Kriging tended to overfit under glider path sampling with low noise levels, leading to an unexpected increase in reconstruction error as the measurement noise grows. In contrast, the TPS maintained stable performance across a wide range of sampling conditions. Given that modern CTD sensors typically have temperature observation errors much below 0.5°C, the aforementioned results suggested that the TPS could offer robust and computationally efficient reconstructions for real glider missions.

The aforementioned findings also confirmed that the proposed TPS-based framework and glider path design remain valid under realistic oceanic conditions, reinforcing their potential utility for guiding future glider missions in complex mesoscale environments. Results for the additional two eddies (Eddy 2 and Eddy 3) provided in Section S4 in the electronic supplementary material were highly consistent with those observed for Eddy 1.

8. Conclusion

This study considers three key aspects of using the underwater gliders for reconstructing the hydrographic field of a mesoscale eddy: interpolation for reconstruction, path design and adaptive path control. With both simulated and real eddy experiments, the proposed TPS interpolation combined with a three-dimensional blocking scheme consistently outperformed IDW and Kriging. For the three real eddy experiments in the Kuroshio Extension, TPS achieved more stable reconstruction accuracy under sparse glider sampling and realistic measurement errors, highlighting its robustness for operational use. For a representative simulated eddy, the TPS method reduced reconstruction errors by 9.3% for temperature and 14.5% for salinity as compared to those by the Kriging.

Our study on the path design offers practical guidance for glider operations by indicating near-optimal deployment numbers and formation strategies. The adaptive control algorithm further ensures robust mission execution in the presence of ocean current, maintaining fidelity to pre-designed paths when currents were weak while guaranteeing destination return under strong currents.

Several limitations should be acknowledged. Operational constraints such as glider availability, battery endurance and communication delays during surfacing may affect the practical deployment of the proposed procedures. Under resource-limited conditions, using only a few gliders may lead to incomplete spatial coverage and reduced reconstruction accuracy. In addition, the adaptive control algorithm depends on reasonably accurate ocean current estimates, which are often difficult to obtain in real time, especially in eddies with intense and highly variable interior currents. Although real-time forecasts from operational systems offer promising mitigation, accurate subsurface current prediction remains an open challenge for glider navigation and control. Moreover, the current path design assumes a quasi-stationary eddy with a stable structure, whereas in reality, eddies often exhibit slow translational motion. Such movement may cause spatial mismatches between planned and actual sampling regions, introducing additional uncertainty into the reconstruction. A further limitation arises from the assumption of vertical smoothness inherent in the TPS interpolation. For eddies exhibiting strong vertical gradients or complex thermocline structures, this assumption may lead to reconstruction biases in the interior layers.

Future research effort should focus on integrating real-time current forecasts into the glider control algorithm and explore hybrid statistical learning with inputs from physical models for real-time glider controls. More broadly, the methodology may be applied to other dynamic oceanographic features, such as internal waves and fronts, to advance in situ observation strategies and to enhance the ability for complex ocean process reconstruction.

Data accessibility. GLORYS ocean reanalysis data are obtained from the Copernicus Marine Service (https://data.marine.copernicus.eu/product/GLOBAL_MULTIYEAR_PHY_001_030/description). The codes used in this study are publicly available at https://github.com/EkkoWusu/Ocean-Glider-Path-Optimization-and-Eddy-Interpolation-Analysis and archived at [82].

The data are provided in the electronic supplementary material [83].

Declaration of AI use. We have not used AI-assisted technologies in creating this article.

Authors' contributions. W.S.: data curation, formal analysis, methodology, visualization, writing—original draft, writing—review and editing; X.E.: formal analysis, methodology, writing—original draft; Z.J.: conceptualization, data curation, project administration, writing—review and editing; S.X.C.: conceptualization, methodology, project administration, writing—review and editing.

All authors gave final approval for publication and agreed to be held accountable for the work performed therein.

Conflict of interest declaration. We declare we have no competing interests.

Funding. This work was supported by the NSFC Major Research Plan on West-Pacific Earth System Multispheric Interactions (grant no. 92358303), and by NSFC grant nos. 12292980 and 12292983. Computational resources were provided by the National Large Scientific and Technological Infrastructure 'Earth System Numerical Simulation Facility'.

References

1. Chelton DB, Schlax MG, Samelson RM. 2011 Global observations of nonlinear mesoscale eddies. *Prog. Oceanogr.* **91**, 167–216. (doi:10.1016/j.pocean.2011.01.002)
2. McGillicuddy DJ, Robinson AR, Siegel DA, Jannasch HW, Johnson R, Dickey TD, McNeil J, Michaels AF, Knap AH. 1998 Influence of mesoscale eddies on new production in the Sargasso Sea. *Nature* **394**, 263–266. (doi:10.1038/28367)
3. Waterman S, Jayne SR. 2011 Eddy-mean flow interactions in the along-stream development of a western boundary current jet: an idealized model study. *J. Phys. Oceanogr.* **41**, 682–707. (doi:10.1175/2010JPO4477.1)
4. Gaube P, McGillicuddy DJ, Chelton DB, Behrenfeld MJ, Strutton PG. 2014 Regional variations in the influence of mesoscale eddies on near-surface chlorophyll. *J. Geophys. Res. Oceans* **119**, 8195–8220. (doi:10.1002/2014JC010111)
5. Zhang Z, Wang W, Qiu B. 2014 Oceanic mass transport by mesoscale eddies. *Science* **345**, 322–324. (doi:10.1126/science.1252418)
6. Griffies SM *et al.* 2015 Impacts on ocean heat from transient mesoscale eddies in a hierarchy of climate models. *J. Clim.* **28**, 952–977. (doi:10.1175/JCLI-D-14-00353.1)
7. Ma X *et al.* 2016 Western boundary currents regulated by interaction between ocean eddies and the atmosphere. *Nature* **535**, 533–537. (doi:10.1038/nature18640)
8. Rohr T, Harrison C, Long M, Gaube P, Doney S. 2020 Eddy-modified iron, light, and phytoplankton cell division rates in the simulated Southern Ocean. *Glob. Biogeochem. Cycles* **34**, e2019GB006380. (doi:10.1029/2019GB006380)
9. Rohr T, Harrison C, Long MC, Gaube P, Doney SC. 2020 The simulated biological response to Southern Ocean eddies via biological rate modification and physical transport. *Glob. Biogeochem. Cycles* **34**, e2019GB006385. (doi:10.1029/2019GB006385)
10. Jing Z *et al.* 2020 Maintenance of mid-latitude oceanic fronts by mesoscale eddies. *Sci. Adv.* **6**, eaba7880. (doi:10.1126/sciadv.aba7880)
11. Chassignet EP *et al.* 2020 Impact of horizontal resolution on global ocean–sea ice model simulations based on the experimental protocols of the Ocean Model Intercomparison Project phase 2 (OMIP-2). *Geosci. Model Dev.* **13**, 4595–4637. (doi:10.5194/gmd-13-4595-2020)
12. Cipollone A, Masina S, Storto A, Iovino D. 2017 Benchmarking the mesoscale variability in global ocean eddy-permitting numerical systems. *Ocean Dyn.* **67**, 1313–1333. (doi:10.1007/s10236-017-1089-5)
13. Moreton SM, Ferreira D, Roberts MJ, Hewitt HT. 2020 Evaluating surface eddy properties in coupled climate simulations with 'eddy-present' and 'eddy-rich' ocean resolution. *Ocean Model.* **147**, 101567. (doi:10.1016/j.ocemod.2020.101567)
14. Dong C, Nencioli F, Liu Y, McWilliams JC. 2011 An automated approach to detect oceanic eddies from satellite remotely sensed sea surface temperature data. *IEEE Geosci. Remote Sens. Lett.* **8**, 1055–1059. (doi:10.1109/LGRS.2011.2155029)
15. Qiu B, Chen S, Klein P, Ubelmann C, Fu LL, Sasaki H. 2016 Reconstructability of three-dimensional upper-ocean circulation from SWOT sea surface height measurements. *J. Phys. Oceanogr.* **46**, 947–963. (doi:10.1175/JPO-D-15-0188.1)
16. Liu L, Xue H, Sasaki H. 2019 Reconstructing the ocean interior from high-resolution sea surface information. *J. Phys. Oceanogr.* **49**, 3245–3262. (doi:10.1175/JPO-D-19-0118.1)
17. Qiu B, Chen S, Klein P, Torres H, Wang J, Fu LL, Menemenlis D. 2020 Reconstructing upper-ocean vertical velocity field from sea surface height in the presence of unbalanced motion. *J. Phys. Oceanogr.* **50**, 55–79. (doi:10.1175/JPO-D-19-0172.1)
18. Liu L, Xue H, Sasaki H. 2021 Diagnosing subsurface vertical velocities from high-resolution sea surface fields. *J. Phys. Oceanogr.* **51**, 1353–1373. (doi:10.1175/JPO-D-20-0152.1)
19. Zhang Z, Zhang Y, Wang W, Huang RX. 2013 Universal structure of mesoscale eddies in the ocean. *Geophys. Res. Lett.* **40**, 3677–3681. (doi:10.1002/grl.50736)
20. Isern-Fontanet J, Lapeyre G, Klein P, Chapron B, Hecht MW. 2008 Three-dimensional reconstruction of oceanic mesoscale currents from surface information. *J. Geophys. Res. Oceans* **113**, C09005. (doi:10.1029/2007JC004692)
21. Shen XR, Wang YH, Yang SQ, Liang Y, Li HZ. 2018 Development of underwater gliders: an overview and prospect. *J. Unmanned Undersea Syst.* **26**, 89–106. (doi:10.11993/j.issn.2096-3920.2018.02.001)

22. Yang M, Wang Y, Wang S, Yang S, Song Y, Zhang L. 2019 Motion parameter optimization for gliding strategy analysis of underwater gliders. *Ocean Eng.* **191**, 106502. (doi:10.1016/j.oceaneng.2019.106502)
23. Wang Y, Zhang L, Liang Y, Yang M, Yang S, Niu W. 2024 Sensitivity analysis of profile navigation command of underwater gliders to the initial heading error for improving trajectory accuracy. *Ocean Eng.* **300**, 117478. (doi:10.1016/j.oceaneng.2024.117478)
24. Zhang Z, Tian J, Qiu B, Zhao W, Chang P, Wu D, Wan X. 2016 Observed 3D structure, generation, and dissipation of oceanic mesoscale eddies in the South China Sea. *Sci. Rep.* **6**, 24349. (doi:10.1038/srep24349)
25. Shepard D. 1968 A two-dimensional interpolation function for irregularly-spaced data. In *Proc. of the 1968 23rd ACM National Conf. ACM '68*, pp. 517–524. New York, NY, USA: Association for Computing Machinery. (doi:10.1145/800186.810616)
26. Matheron G. 1963 Principles of geostatistics. *Econ. Geol.* **58**, 1246–1266. (doi:10.2113/gsecongeo.58.8.1246)
27. Hevesi JA, Istok JD, Flint AL. 1992 Precipitation estimation in mountainous terrain using multivariate geostatistics. 1. Structural-analysis. *J. Appl. Meteorol.* **31**, 661–676. (doi:10.1175/1520-0450(1992)0312.0.CO;2)
28. Nalder IA, Wein RW. 1998 Spatial interpolation of climatic normals: test of a new method in the Canadian boreal forest. *Agric. For. Meteorol.* **92**, 211–225. (doi:10.1016/S0168-1923(98)00102-6)
29. Cressie N. 1993 3. In *Spatial prediction and kriging*, pp. 105–209. Hoboken, NJ: John Wiley & Sons, Ltd. (doi:10.1002/9781119115151.ch3)
30. Li S, Zhang F, Wang S, Wang Y, Yang S. 2020 Constructing the three-dimensional structure of an anticyclonic eddy with the optimal configuration of an underwater glider network. *Appl. Ocean Res.* **95**, 101893. (doi:10.1016/j.apor.2019.101893)
31. Hutchinson MF, de Hoog FR. 1985 Smoothing noisy data with spline functions. *Numer. Math.* **47**, 99–106. (doi:10.1007/BF01389878)
32. Wahba G, Wendelberger J. 1980 Some new mathematical methods for variational objective analysis using splines and cross validation. *Mon. Weather Rev.* **108**, 1122–1143. (doi:10.1175/1520-0493(1980)108<1122:SNMMFV>2.0.CO;2)
33. Hutchinson MF, Gessler PE. 1994 Splines–more than just a smooth interpolator. *Geoderma* **62**, 45–67. (doi:10.1016/0016-7061(94)90027-2)
34. Zheng X, Basher R. 1995 Thin-plate smoothing spline modeling of spatial climate data and its application to mapping south pacific rainfalls. *Mon. Weather Rev.* **123**, 3086–3102. (doi:10.1175/1520-0493(1995)123¡3086:TPSSMO¿2.0.CO;2)
35. Leonard NE, Paley DA, Lekien F, Sepulchre R, Davis RE. 2007 Collective motion, sensor networks, and ocean sampling. *Proc. IEEE* **95**, 48–74. (doi:10.1109/JPROC.2006.887295)
36. Alvarez A, Garau B, Caiti A. 2007 Combining networks of drifting profiling floats and gliders for adaptive sampling of the Ocean. In *Proc. 2007 IEEE Int. Conf. on Robotics and Automation*, pp. 157–162. New York, NY: IEEE. (doi:10.1109/ROBOT.2007.363780)
37. Alvarez A, Mourre B. 2012 Optimum sampling designs for a glider-mooring observing network. *J. Atmos. Oceanic Technol.* **29**, 601–612. (doi:10.1175/JTECH-D-11-00105.1)
38. Sang H, Ying Z, Sun X, Yang S. 2018 Heading tracking control with an adaptive hybrid control for under actuated underwater glider. *ISA Trans.* **80**, 554–563. (doi:10.1016/j.isatra.2018.06.012)
39. Garau B, Castillo Bonet M, Alvarez A, Ruiz S, Pascual A. 2009 Path planning for autonomous underwater vehicles in realistic oceanic current fields: application to gliders in the Western Mediterranean Sea. *J. Marit. Res.* **6**, 5–22. (doi:10.1109/TRO.2007.895057)
40. Besada-Portas E, Moreno A, Risco-Martín JL. 2013 On the performance comparison of multi-objective evolutionary UAV path planners. *Inf. Sci.* **238**, 111–125. (doi:10.1016/j.ins.2013.02.022)
41. Zamuda A, Hernández Sosa JD. 2014 Differential evolution and underwater glider path planning applied to the short-term opportunistic sampling of dynamic mesoscale ocean structures. *Appl. Soft Comput.* **24**, 95–108. (doi:10.1016/j.asoc.2014.06.048)
42. Zamuda A, Hernández Sosa JD, Adler L. 2016 Constrained differential evolution optimization for underwater glider path planning in sub-mesoscale eddy sampling. *Appl. Soft Comput.* **42**, 93–118. (doi:10.1016/j.asoc.2016.01.038)

43. Zamuda A. 2017 Adaptive constraint handling and success history differential evolution for CEC 2017 constrained real-parameter optimization. In *Proc. IEEE Congr. Evol. Comput.*, pp. 2443–2450. New York, NY: IEEE. (doi:10.1109/CEC.2017.7969601)
44. Zamuda A, Sosa JDH. 2019 Success history applied to expert system for underwater glider path planning using differential evolution. *Expert Syst. Appl.* **119**, 155–170. (doi:10.1016/j.eswa.2018.10.048)
45. Wang C, Li W, Wang Z, Song M, Mahmoudian N. 2018 Reinforcement learning-based adaptive trajectory planning for AUVs in under-ice environments. In *OCEANS 2018 MTS/IEEE Charleston*, pp. 1–6. New York, NY: IEEE. (doi:10.1109/OCEANS.2018.8604754)
46. Ma X, Wang Y, Yang S, Niu W, Ma W. 2021 Trajectory tracking of an underwater glider in current based on deep reinforcement learning. In *OCEANS 2021: San Diego—Porto*, pp. 1–7. New York, NY: IEEE. (doi:10.23919/OCEANS44145.2021.9705882)
47. Hijmans RJ, Cameron SE, Parra JL, Jones PG, Jarvis A. 2005 Very high resolution interpolated climate surfaces for global land areas. *Int. J. Climatol.* **25**, 1965–1978. (doi:10.1002/joc.1276)
48. Bookstein FL. 1989 Principal warps: thin-plate splines and the decomposition of deformations. *IEEE Trans. Pattern Anal. Mach. Intell.* **11**, 567–585. (doi:10.1109/34.24792)
49. Guo J, Nie Y, Li S, Lv X. 2020 Application of three-dimensional interpolation in estimating diapycnal diffusivity in the South China Sea. *J. Mar. Sci. Eng.* **8**, 832. (doi:10.3390/jmse8110832)
50. Tang Z, Chen K, Pan M, Wang M, Song Z. 2019 An augmentation strategy for medical image processing based on statistical shape model and 3D thin plate spline for deep learning. *IEEE Access* **7**, 133111–133121. (doi:10.1109/ACCESS.2019.2941154)
51. Zhang Z, Wang G, Wang H, Liu H. 2024 Three-dimensional structure of oceanic mesoscale eddies. *Ocean-Land-Atmos. Res.* **3**, 0051. (doi:10.34133/olar.0051)
52. Zhang W, Griffies SM, Hallberg RW, Kuo YH, Wolfe CLP. 2024 The role of surface potential vorticity in the vertical structure of mesoscale eddies in wind-driven ocean circulations. *J. Phys. Oceanogr.* **54**, 1243–1266. (doi:10.1175/JPO-D-23-0203.1)
53. Wahba G. 1990 *Spline models for observational data*. Philadelphia: Society for Industrial and Applied Mathematics, SIAM.
54. Yang M, Wang Y, Zhang X, Liang Y, Wang C. 2023 Parameterized dynamic modeling and spiral motion pattern analysis for underwater gliders. *IEEE J. Ocean. Eng.* **48**, 112–126. (doi:10.1109/JOE.2022.3181896)
55. Xue DY, Wu ZL, Wang YH, Wang SX. 2018 Coordinate control, motion optimization and sea experiment of a fleet of petrel-II gliders. *Chin. J. Mech. Eng.* **31**, 17. (doi:10.1186/s10033-018-0210-0)
56. Stark JD, Donlon CJ, Martin MJ, McCulloch ME. 2007 OSTIA: an operational, high resolution, real time, global sea surface temperature analysis system. In *OCEANS 2007—Europe*, pp. 1–4. New York, NY: IEEE. (doi:10.1109/OCEANSE.2007.4302251)
57. Mecklenburg S *et al.* 2016 ESA's soil moisture and ocean salinity mission: from science to operational applications. *Remote Sens. Environ.* **180**, 3–18. (doi:10.1016/j.rse.2015.12.025)
58. Pascual A, Faugére Y, Larnicol G, Le Traon PY. 2006 Improved description of the ocean mesoscale variability by combining four satellite altimeters. *Geophys. Res. Lett.* **33**, L02611. (doi:10.1029/2005GL024633)
59. Melnichenko O, Amores A, Maximenko N, Hacker P, Potemra J. 2017 Signature of mesoscale eddies in satellite sea surface salinity data. *J. Geophys. Res. Oceans* **122**, 1416–1424. (doi:10.1002/2016JC012420)
60. Cummings JA. 2005 Operational multivariate ocean data assimilation. *Q. J. R. Meteorol. Soc.* **131**, 3583–3604. (doi:10.1256/qj.05.105)
61. Cummings JA, Smedstad OM. 2013 Variational data assimilation for the global ocean. In *Data assimilation for atmospheric, oceanic and hydrologic applications* (vol. II), pp. 303–343. Berlin. Germany: Springer. (doi:10.1007/978-3-642-35088-7_13)
62. Small RJ *et al.* 2014 A new synoptic scale resolving global climate simulation using the community earth system model. *J. Adv. Model. Earth Syst.* **6**, 1065–1094. (doi:10.1002/2014MS000363)
63. Zhou Y, Yu J, Wang X. 2014 Path planning method of underwater glider based on energy consumption model in current environment. In *Intelligent robotics and applications*, pp. 142–152. Cham, Switzerland: Springer International Publishing. (doi:10.1007/978-3-319-13966-1_14)
64. Liu Y, Su Z, Luan X, Song D, Han L. 2017 Motion analysis and fuzzy-PID control algorithm designing for the pitch angle of an underwater glider. *J. Math. Comput. Sci.* **17**, 133–147. (doi:10.22436/jmcs.017.01.12)

65. Ullah B, Ovinis M, Baharom MB, Javaid MY, Izhar SS. 2015 Underwater gliders control strategies: a review. In *2015 10th Asian Control Conf. (ASCC)*, pp. 1–6. New York, NY: IEEE. (doi:10.1109/ASCC.2015.7244859)
66. Cui Y *et al.* 2025 Forecasting the eddying ocean with a deep neural network. *Nat. Commun.* **16**, 2268. (doi:10.1038/s41467-025-57389-2)
67. Oke PR, Brassington GB, Griffin DA, Schiller A. 2008 The bluelink ocean data assimilation system (BODAS). *Ocean Model.* **21**, 46–70. (doi:10.1016/j.ocemod.2007.11.002)
68. Liu F, Wang YH, Wu ZL, Wang SX. 2017 Motion analysis and trials of the deep sea hybrid underwater glider Petrel-II. *Chin. Ocean Eng.* **31**, 55–62. (doi:10.1007/s13344-017-0007-4)
69. Rudnick DL. 2016 Ocean research enabled by underwater gliders. *Annu. Rev. Mar. Sci.* **8**, 519–541. (doi:10.1146/annurev-marine-122414-033913)
70. Wahba G. 1990 *Spline models for observational data*. Philadelphia, PA: Society for Industrial and Applied Mathematics.
71. Brest J, Greiner S, Boskovic B, Mernik M, Zumer V. 2006 Self-adapting control parameters in differential evolution: a comparative study on numerical benchmark problems. *IEEE Trans. Evol. Comput.* **10**, 646–657. (doi:10.1109/TEVC.2006.872133)
72. Zhu L, Ma Y, Bai Y. 2020 A self-adaptive multi-population differential evolution algorithm. *Nat. Comput.* **19**, 211–235. (doi:10.1007/s11047-019-09757-3)
73. Kennedy J, Eberhart R. 1995 Particle swarm optimization. In *Proc. of ICNN'95—Int. Conf. on Neural Networks*, vol. 4, pp. 1942–1948. New York, NY: IEEE. (doi:10.1109/ICNN.1995.488968)
74. Wang S, Li Y, Yang H. 2019 Self-adaptive mutation differential evolution algorithm based on particle swarm optimization. *Appl. Soft Comput.* **81**, 105496. (doi:10.1016/j.asoc.2019.105496)
75. Inanc T, Shadden SC, Marsden JE. 2005 Optimal trajectory generation in ocean flows. In *Proc. of the 2005 American Control Conf.*, pp. 674–679. New York, NY: IEEE. (doi:10.1109/ACC.2005.1470035)
76. Sun H, Song Q, Shao R, Schlicke T. 2016 Estimation of sea surface currents based on ocean colour remote-sensing image analysis. *Int. J. Remote Sens.* **37**, 5105–5121. (doi:10.1080/01431161.2016.1226526)
77. Allotta B, Costanzi R, Fanelli F, Monni N, Paolucci L, Ridolfi A. 2017 Sea currents estimation during AUV navigation using Unscented Kalman Filter. *IFAC-Pap. Online* **50**, 13 668–13 673. (doi:10.1016/j.ifacol.2017.08.2528)
78. Zhu Y, Liang X. 2020 Coupling of the surface and near-bottom currents in the Gulf of Mexico. *J. Geophys. Res. Oceans* **125**, e2020JC016488. (doi:10.1029/2020JC016488)
79. Purkiani K, Paul A, Vink A, Walter M, Schulz M, Haeckel M. 2020 Evidence of eddy-related deep-ocean current variability in the northeast tropical Pacific Ocean induced by remote gap winds. *Biogeosciences* **17**, 6527–6544. (doi:10.5194/bg-17-6527-2020)
80. Wang J, Flierl GR, LaCasce JH, McClean JL, Mahadevan A. 2013 Reconstructing the ocean's interior from surface data. *J. Phys. Oceanogr.* **43**, 1611–1626. (doi:10.1175/JPO-D-12-0204.1)
81. Taburet G, Sanchez-Roman A, Ballarotta M, Pujol MI, Legeais JF, Fournier F, Faugere Y, Dibarboure G. 2019 DUACS DT2018: 25 years of reprocessed sea level altimetry products. *Ocean Sci.* **15**, 1207–1224. (doi:10.5194/os-15-1207-2019)
82. Su W. 2026 EkkoWusu/ocean-glider-path-optimization-and-eddy-interpolation-analysis: ocean glider path optimization and eddy interpolation analysis. Zenodo. (doi:10.5281/zenodo.18257057)
83. Su W, E X, Jing Z, Chen SX. 2026 Glider path design and control for reconstructing three-dimensional structures of oceanic mesoscale eddies. Figshare. (doi:10.6084/m9.figshare.c.8316008)